

148
NASA CR-130149

**FINITE ELEMENT SOLUTION FOR ENERGY CONSERVATION USING A HIGHLY
STABLE EXPLICIT INTEGRATION ALGORITHM**

A. J. Baker
Paul D. Manhardt
Bell Aerospace Company
P. O. Box One
Buffalo, New York 14240

October 1972
Final Technical Report — June - October 1972

Prepared for
GODDARD SPACE FLIGHT CENTER
Greenbelt, Maryland 20771

Reproduced by
**NATIONAL TECHNICAL
INFORMATION SERVICE**
US Department of Commerce
Springfield, VA. 22151



(NASA-CR-130149) **FINITE ELEMENT SOLUTION
FOR ENERGY CONSERVATION USING A HIGHLY
STABLE EXPLICIT INTEGRATION ALGORITHM**
Final Technical Report, Jun. - (Bell
Aerospace Co.) 56 p HC

N73-16593

C5CL 12A

G3/19

**Unclas
53656**

1. Report No. NASA CR-	2. Government Accession No.	3. Recipient's Catalog No.	
4. Title and Subtitle Finite Element Solution for Energy Conservation Using A Highly Stable Explicit Integration Algorithm		5. Report Date October, 1972	
		6. Performing Organization Code	
7. Author(s) A.J. Baker and Paul D. Manhardt		8. Performing Organization Report No. 9500-920257	
9. Performing Organization Name and Address Bell Aerospace Company P.O. Box One Buffalo, New York 14240		10. Work Unit No.	
		11. Contract or Grant No. NAS5-11935	
12. Sponsoring Agency Name and Address Dr. H. P. Lee, Technical Monitor Goddard Space Flight Center Greenbelt, Maryland 20771		13. Type of Report and Period Covered Final Technical Report June - October, 1972	
		14. Sponsoring Agency Code	
15. Supplementary Notes			
16. Abstract <p>This contract final technical report presents the theoretical derivation of a finite element solution algorithm for the transient energy conservation equation in multidimensional, stationary multi-media continua with irregular solution domain closure. It establishes the complete finite element matrix forms for arbitrarily irregular discretizations using natural co-ordinate function representations. It describes embodiment of the algorithm into a user-oriented computer program (COMOC) which obtains transient temperature distributions at the node points of the finite element discretization using a highly stable explicit integration procedure with automatic error control features. The finite element algorithm is shown to possess convergence with discretization for a transient sample problem. The condensed form for the specific heat element matrix is shown to be preferable to the consistent form. Sample results computed for a practical aerospace problem indicate excellent solution accuracy and speed of computation, and factors within the integration package which affect its operation are evaluated. Computed results for diverse problems illustrate the versatility of COMOC, and easily prepared output sub-routines are shown to allow quick engineering assessment of solution behavior.</p>			
17. Key Words Finite Element Numerical Integration Heat Conduction Continuum Mechanics		18. Distribution Statement	
19. Security Classif. (of this report) Unclassified	20. Security Classif. (of this page) Unclassified	21. No. of Pages 50	22. Price

ABSTRACT

This contract final technical report presents the theoretical derivation of a finite element solution algorithm for the transient energy conservation equation in multidimensional, stationary multi-media continua with irregular solution domain closure. It establishes the complete finite element matrix forms for arbitrarily irregular discretizations using natural coordinate function representations. It describes embodiment of the algorithm into a user-oriented computer program (COMOC) which obtains transient temperature distributions at the node points of the finite element discretization using a highly stable explicit integration procedure with automatic error control features. The finite element algorithm is shown to possess convergence with discretization for a transient sample problem. The condensed form for the specific heat element matrix is shown to be preferable to the consistent form. Sample results computed for a practical aerospace problem indicate excellent solution accuracy and speed of computation, and factors within the integration package which affect its operation are evaluated. Computed results for diverse problems illustrate the versatility of COMOC, and easily prepared output subroutines are shown to allow quick engineering assessment of solution behavior.

CONTENTS

Section		Page
I	INTRODUCTION	1
II	FINITE ELEMENT SOLUTION ALGORITHM FOR ENERGY CONSERVATION	2
	A. Governing Differential Equations	2
	B. Finite Element Solution Algorithm	3
	C. Finite Element Matrix Generation	7
	1. Planar Elements in Two-Dimensional Space	7
	2. Planar Ring Elements in Axisymmetric Two-Dimensional Space	11
III	HIGHLY STABLE EXPLICIT NUMERICAL INTEGRATION ALGORITHM.....	12
IV	FINITE ELEMENT COMPUTER PROGRAM	15
V	NUMERICAL RESULTS	16
	A. Accuracy and Convergence with Discretization	16
	B. Accuracy and Solution Speed for a Practical Engineering Problem	22
	C. Versatility Illustration for COMOC	39
VI	CONCLUSIONS AND RECOMMENDATIONS	47
VII	REFERENCES	49

ILLUSTRATIONS

Figure		Page
1.	Finite Element Shapes for Linear Approximation Functions	6
2.	COMOC Computer Program Organization	15
3.	Discretization of Thick Axisymmetric Cylinder into Thirty-Two Triangular Cross-Section Ring Finite Elements	18
4.	Accuracy Comparison of Computed Transient Temperature Distributions in Thick Axisymmetric Cylinder As Function of [C] Form and Discretization	20
5.	Comparison of Surface Temperature and Integration Step-Size for Different Integration Methods and Matrix Forms for Thirty-Two Element Cylinder Discretization	21
6.	Transient Surface Temperature of Thick Axisymmetric Cylinder as Function of Thermal Conductivity, Epsilon = 0.01, Method 2, Condensed Matrix	23
7.	Discretization of Axisymmetric Rocket Motor Into 104 Triangular Cross-Section Ring Finite Elements	25
8.	Comparison of Computed Axial Temperature Distributions After Ten Second Firing of Rocket Motor	26
9.	Comparison of Computed Transient Temperature Distribution at Nozzle Throat of Rocket Motor During Ten Second Firing	28
10.	Computed Temperature Distribution Within Rocket Motor After One Second Firing, 104 Finite Element Discretization	29
11.	Discretization of Axisymmetric Rocket Motor Into 538 Finite Element Discretization Cross-Section Ring Finite Elements	30
12.	Computed Temperature Distribution Within Rocket Motor After One Second Firing, 538 Finite Element Discretization	31
13.	Computed Radial Temperature Distributions Through Rocket Nozzle Throat and Combustion Chamber After One Second Firing	32
14.	Comparison of Computed Transient Temperature Distribution at the Nozzle Throat for QKNINT Method 1 and Euler, 538 Finite Element Discretization	34
15.	Comparison of Surface Temperature Distribution and Integration Sep-Size History for QKNINT (1) and Euler, 104 and 538 Finite Element Discretizations, Epsilon = 0.01	35
16.	Computed Temperature Distribution Within Rocket Motor After Nine Second Firing Using Euler Integration Algorithm	36
17.	Computed Temperature Distribution Within Rocket Motor After Nine Second Firing Using QKNINT (1) Integration Algorithm	37
18.	Solution Speed as Function of HMIN Seeking Factor for Automatic Operation Mode of QKNINT	40
19.	Computed Temperature Distribution in Two-Dimensional Analog of Axisymmetric Rocket Motor Problem	41
20.	Radial Temperature Distribution Comparison for Graphite Insert and Stainless Steel Rocket Motor	43
21.	Computed Rocket Motor Surface Temperature Distributions After 10 Second Firing for Isotropic and Orthotropic Thermal Conductivities	44
22.	Axial Surface Temperature Distribution 10 Seconds After Welding Operation on Segment of Wedge Shaped Domain	46

TABLES

Number		Page
1.	Implicit Definition of Linear Natural Coordinate Functions	8
2.	Integrals of the Natural Coordinate Functions	8
3.	Finite Element Matrices for the Energy Conservation Equation Solution Algorithm	10
4.	Coefficients in Finite Difference Integration Algorithm, Euqation 3.1, for Two, One-Step, Three-Stage Methods	14
5.	Transient Temperature Distributions in Thick Axisymmetric Cylinder	19
6.	Comparison of Solution Speed for QKNINT (1) and Euler Integration, Epsilon = 0.01	38
7.	Computed Radial Temperature Distribution Along Node Line α , Figure 7, for Simulated Active Cooling of Rocket Motor After 10 Second Firing	45

I. INTRODUCTION

Numerical solution of the discretized equivalent of the initial boundary value problem of mathematical physics is commonplace with the advent of the large digital computer. The finite element method, well proven for solution of large-scale problems in structural mechanics, is being extended to general boundary value problems throughout continuum mechanics. For these problems in heat transfer, fluid mechanics, electromagnetic theory, and magneto hydrodynamics, application of the finite element solution algorithm to the original system of quasilinear partial differential equations produces large-order systems of ordinary differential equations written on the discretized equivalent of the original dependent variables. These equations are eligible for solution by both implicit and explicit numerical integration techniques.

Recent research has yielded analytical techniques for deriving integration methods for ordinary differential equations that are optimum on the multiple bases of stability, accuracy and required computing time. Computational methods are available for establishing specifically tailored 1-, 2-, and 3-step explicit integration algorithms, satisfying both accuracy and stability requirements if possible. These techniques have been used to establish a class of explicit numerical integration methods which are one-step (and therefore self-starting), have error control features, require derivative evaluations at the integration-interval end points only, are optimally stable and accurate within their given structure, and are readily programmed for use on the digital computer. These methods represent a generalization of the well known one-step predictor-corrector methods with 2 corrections and 3 derivative evaluations per step.

The results of numerical evaluation of the highly stable integration algorithm are presented herein as established via solution of the ordinary differential equation system resulting from a simplex finite element discretization of two-dimensional and axisymmetric problems in transient heat transfer. These results corroborate the theoretical predictions and illustrate the usefulness of the automatic error control features. The versatility of the finite element solution technique is similarly exemplified for practical problems involving complex geometries, tensor conductivities, and temperature dependent thermophysical properties.

II. FINITE ELEMENT SOLUTION ALGORITHM FOR ENERGY CONSERVATION

A. GOVERNING DIFFERENTIAL EQUATIONS

The fundamental concept in continuum mechanics analysis is identification of material distributions over domains, and satisfaction of the conservation laws of mechanics expressed in terms of the continuum distributions. For a bounded domain at rest in an inertial reference frame, containing material of constant but non-uniform density, the conservation laws not identically satisfied reduce to the first and second laws of thermodynamics. In its elementary form, the first law of thermodynamics states

$$\Delta E = \Delta Q - \Delta W \quad (2.1)$$

where ΔE is the energy change within a domain when ΔQ amount of heat has been added and ΔW amount of work has been done. Averaging Eq (2.1) over a time interval Δt and taking the limit as Δt approaches zero, we have, assuming the limit exists and is finite, the equivalent differential equation statement of the first law.

$$\frac{dE}{dt} = \frac{dQ}{dt} - \frac{dW}{dt} \quad (2.2)$$

In the context of the present development, the second law of thermodynamics places a lower limit on allowed entropy changes between thermodynamic end points.

Eq (2.2) is valid over all domains. It can be specialized to a continuum distribution by identification of appropriate thermodynamic and material variables. The internal energy E is expressed in terms of a corresponding internal energy density, e , as

$$E \equiv \int_R \rho e d\tau \quad (2.3)$$

The thermodynamic point function, e , can be expressed as a function of two other variables, say density and temperature. Since density is at least piecewise constant, and identifying a specific heat capacity, c , obtain for the internal energy density.

$$e = \int^T c(T) dT \quad (2.4)$$

Considering the remaining terms in Eq (2.2), the work done by an incompressible continuum at rest is zero. The heat-added term may have contributions stemming from internal generation, \dot{Q} , and a net inward flux of heat, q_i , over the bounding surface ∂R of the domain R . Concerning the latter, it is convenient to relate forces and resultant fluxes by material coefficients. Accounting for the vector character of heat flux and temperature gradient, the material property flux coefficient can at most be a second-order tensor. Using Cartesian tensor subscript notation, with the summation convention implied for repeated Latin indices and partial differentiation denoted by a comma, the generalized flux form is

$$q_i = k_{ij} T_{,j} \quad (2.5)$$

where k_{ij} , the thermal conductivity tensor, is typically temperature-dependent for practical problems.

Employing the defined material properties, and the concept of mass distribution, the first law of thermodynamics, Eq (2.2), can be written as an integro-differential equation of the form

$$\oint_{\partial R} k_{ij} T_{,j} n_i d\sigma + \int_R \rho \dot{Q} d\tau = \frac{d}{dt} \int_R \int^T \rho c dT d\tau \quad (2.6)$$

Employing Gauss' theorem on the surface integral, and noting that the domain R is time independent and arbitrary, the integrand must vanish identically. The familiar differential equation for energy conservation at a point is then

$$(k_{ij} T_{,j})_{,i} + \rho \dot{Q} = \rho c T_{,t} \quad (2.7)$$

With the explicit assumption that material properties can be discontinuous, Eq (2.7) is valid throughout R by subdomains with boundaries identical with the surfaces of these discontinuities.

Equation (2.7) is an elliptic boundary value problem that is also initial value. Hence, a unique solution exists for appropriate specification of boundary and initial conditions. The initial condition is simply

$$T(x_i, 0) = T_0(x_i) \quad (2.8)$$

The generalized elliptic boundary condition is a first order differential equation relating the temperature and its normal derivative, on the complete closure of the domain R, of the form

$$a_1(t) T(\bar{x}_i, t) + a_2(t) T(\bar{x}_i, t)_{,k} n_k = a_3(t) \quad (2.9)$$

In Eq (2.9), should a_1 vanish on any closure segment, a fixed heat flux is applied to that portion of the domain closure. The vanishing of a_2 enforces a fixed temperature. Should none of the a_i vanish, the temperature and its normal gradient are linearly related, the so-called convection boundary condition, usually written as

$$q_i(\bar{x}_i, t) \equiv h(\bar{x}_i, t) [T(\bar{x}_i, t) - T_r(\bar{x}_i, t)] n_i \quad (2.10)$$

where h is the defined convective heat transfer coefficient and T_r is the temperature of the reference exchange medium.

Another form of surface energy flux with the domain of interest, requiring no close communication with the source, is radiant energy exchange. This boundary condition statement is similar to Eq (2.10), but with fourth power appearance of the temperature terms and generalization of the heat transfer coefficient to include geometric viewfactors. The temperature quartic can be factored once to yield Eq (2.10) explicitly, with the following expression resulting for the radiation heat transfer coefficient.

$$h_r(\bar{x}_i, t) = \sigma \alpha(\bar{x}_i, t) [T^3 + T^2 T_r + T T_r^2 + T_r^3] \quad (2.11)$$

In Eq (2.11), σ is the Stefan - Boltzmann constant and α is the viewfactor. Eq (2.9) is thus noted to embody both of the familiar convection and radiation boundary condition forms.

B. FINITE ELEMENT SOLUTION ALGORITHM

For a numerical solution algorithm of the equation system (2.7) - (2.9) to be practical, it must explicitly admit variable thermophysical properties and arbitrarily shaped solution domain closures. The finite element procedure is distinctly appropriate for this purpose. Use is made of Galerkin criteria in the Method of Weighted Residuals (MWR), on a local basis, to provide the theoretical foundation for the finite element solution algorithm.

Equation (2.7), a quasilinear elliptic partial differential equation, can be written in the form

$$L(T) \equiv (k_{ij} T, j)_{,i} + f(T, T, j, x_i, t) = 0 \quad (2.12)$$

Classical application of Galerkin criteria within MWR constitutes forming an approximation, $T^*(x_i, t)$ to the dependent variable, $T(x_i, t)$, by a series expansion into a set of unknown coefficients modifying members, ϕ_k , of a complete set of functions in the spatial variables.

$$T^*(x_i, t) \equiv \sum_{k=1}^K C_k(t) \phi_k(x_i) \quad (2.13)$$

Certain of these expansion coefficients are evaluated by requiring that the approximate solution satisfy the boundary conditions, Eq. (2.9). The remaining unknown coefficients are then determined by setting to zero the differential equation residuals, formed by substitution of T^* into Eq (2.12), multiplication by a set of weighting functions, W_k , typically identical to the spatial approximation functions, ϕ_k , and integrating over the domain R . This produces the N ordinary differential (or algebraic, for a time independent problem) equations

$$\int_R W_k(x_i) L(T^*) d\tau \equiv 0 \quad k = 1, 2, \dots, N \quad (2.14)$$

where N corresponds to the total number of remaining unknown coefficients in the definition of the approximation function, Eq (2.13).

When non-vanishing gradient boundary conditions exist, a generalization to the classical MWR approach is advantageous, to relax the constraints formed by the boundary condition statement, Eq (2.9). Form the N boundary residuals, after generalization of a_2 , Eq. (2.9), as

$$\int_{\partial R} W_k(x_i) [T^* - \frac{1}{a_1} (a_3 - a_{2ij} T, j n_i)] d\sigma \equiv 0 \quad k = 1, 2, \dots, N \quad (2.15)$$

Looking to the variational calculus for guidance, multiply Eq (2.15) by a Lagrange multiplier, λ , and subtract them from Eq. (2.14). Noting that the N weighting functions can be written as,

$$W_k(x_i) = \frac{\partial T^*(x_i, t)}{\partial C_k(t)} \quad (2.16)$$

integrating by parts the differential equation term involving the elliptic operator, identifying λ with unity, and specifying that a_2 coincide with the thermal conductivity tensor, a cancellation of terms is achieved. The resultant equation system for determination of the remaining expansion coefficients in Eq. (2.13) becomes

$$\int_R \left(\frac{\partial T^*}{\partial C_k} \right)_{,j} (k_{ij} T^*_{,i}) d\tau + \int_R \frac{\partial T^*}{\partial C_k} f(T^*, T^*_{,i}, x_i, t) d\tau - \int_{\partial R} \frac{\partial T^*}{\partial C_k} [a_1 T^* - a_3] d\sigma = 0$$

$$k = 1, 2, \dots, N \quad (2.17)$$

It is readily shown that Eq (2.17) is identical to that equation formed by extremization of the variational equivalent statement of Eq (2.7) - (2.9), when the equations are linear and f is explicitly independent of both T and t .

The Numerical Method of Weighted Residuals follows directly from this theory. Form a series approximation, T_m^* , to the dependent variable, T , constrained to lie within the m^{th} subdomain, R_m , defined by $(x_i, t) \in R_m \times [0, \infty)$, and where the union of the M disjoint interior subdomains, R_m , forms R . Evaluate Eq (2.17) in each of these "finite elements", R_m , applying the gradient boundary condition statement to those elements with surfaces coincident with the solution domain closure ∂R . Assemble the $M \times N$ Eq (2.17) into a global system written on the totality of unconstrained expansion coefficients, $C_{mk}(t)$, by Boolean algebra. The equation system thus produced is again identical to that formed by a variational procedure when a stationary principle exists for Eq (2.7) - (2.9), i.e., when the differential equation system is linear and time-independent. However, since no linearity constraint has been employed in the derivation of the solution theory, it is generally applicable to all problem descriptions belonging to Eq (2.7) - (2.9).

The final step for establishment of the finite element solution algorithm is selection of the functionals, $\phi_k(x_i)$, Eq (2.13), and determination of the desired shape of the discretized subdomains, R_m . The vast experience in structural analysis has yielded finite element shapes and approximation functions which are highly specialized to each particular problem class. At this juncture, for the energy conservation problem, it appears that use of low order polynomials spanning the space of the subdomain can provide sufficiently accurate and economical solutions for practical engineering problems.

The further restriction that $\phi_k(x_i)$ be linear polynomials establishes the finite element shapes shown in Figure 1 for 1-, 2- and 3-dimensional spaces respectively. Selecting node locations on the closure of the subdomain, ∂R_m , as indicated, allows physical significance to be attached to the expansion coefficients, Eq (2.13), by requiring that the series represent (dimensionally) the temperature at each node. With this specialization, the approximation to temperature in the m^{th} finite element takes the form

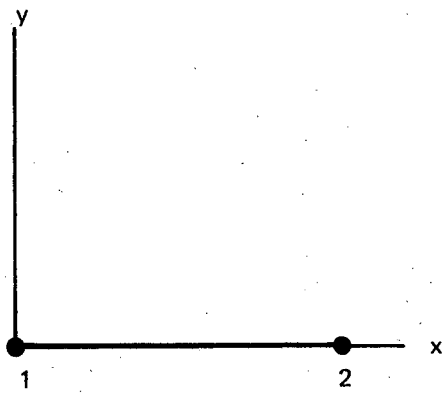
$$T_m^*(x_i, t) = \{L\}^T \{\theta(t)\}_m \quad (2.18)$$

The elements of the vector $\{\theta(t)\}$ are the time dependent temperatures at nodes of the discretization and the elements of $\{L\}$ are linear polynomials in the spatial coordinates. With identification of Eq (2.18) the weighting functions, Eq (2.16), for Galerkin criteria are simply the elements of $\{L\}$. Combining Eq (1.27) - (2.18), the finite element solution algorithm for Eq (2.7) - (2.9), within the finite element R_m , can be compactly written as

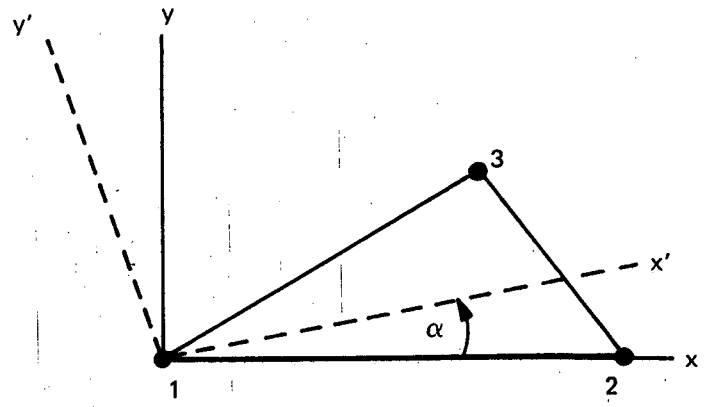
$$[C]_m \{\theta(t)\}_m = - \sum_I [K1]_m \{\theta(t)\}_m + \sum_I \{Y1\}_m \quad (2.19)$$

by identification of the following element matrices.

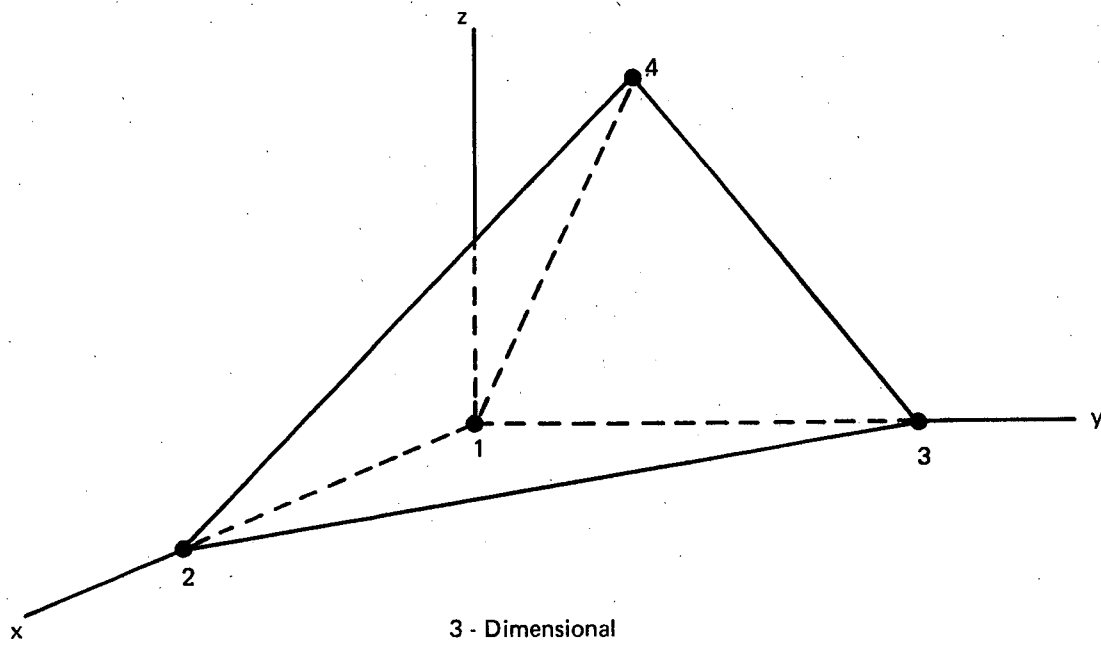
$$\begin{aligned} [C]_m &\equiv \int_{R_m} \{L\} \rho_m c_m \{L\}^T d\tau \\ [K1]_m &\equiv \int_{R_m} \{L\} \cdot_j [k_{ij}^m] \{L\}^T \cdot_i d\tau \\ [K2]_m &\equiv \int_{\partial R_m} \{L\} a_{1m} \{L\}^T d\sigma \\ \{Y1\}_m &\equiv \int_{R_m} \{L\} \rho_m \dot{Q}_m d\tau \\ \{Y2\}_m &\equiv \int_{\partial R_m} \{L\} a_{3m} d\sigma \end{aligned} \quad (2.20)$$



1 - Dimensional



2 - Dimensional



3 - Dimensional

Figure 1. Finite Element Shapes for Linear Approximation Functions

In Eq (2.19) the superscript prime denotes the ordinary time derivative of the element vector of nodal temperatures. The finite element matrices defined in Eq (2.20) are respectively the specific heat capacity, the thermal conductivity, the temperature dependent contribution to the flux boundary condition, the internal heat generation, and the temperature independent contribution to the flux boundary condition.

Equations of the form (2.19) are written for every finite element lying within the solution domain. Assembly by Boolean algebra of the M Eq (2.19), into the required global solution form, yields an equation system which is identical in appearance, save for deletion of the subscript m. Global equation (2.19) is formally rendered in standard form, for solution by any (finite difference) integration algorithm, by pre-multiplication with $[C]^{-1}$, the inverse of the global heat capacity matrix. Thus the final form of the finite element solution algorithm for the time dependent distribution of node temperatures of the discretization becomes

$$\{\theta(t)\}' = [C]^{-1} \left(- \sum_I [KI] \{\theta(t)\} + \sum_I \{YI\} \right) \quad (2.21)$$

Boundary condition specifications are accepted on an element basis by the set of a_{jm} , Eq (2.9), for each finite element with nodes occurring on the closure of the global solution domain. For a typical element, should a_{1m} be zero, the boundary temperature gradient is prescribed (fixed heat flux) and accounted for by $\{Y2\}$, Eq (2.20). Should a_{2m} vanish identically, the node temperature is fixed and not calculable from Eq (2.21). Finally, if none of the a_{jm} vanish, the contributions are contained within both the $\{Y2\}$ and $[K2]$ matrices, Eq (2.20). The more familiar convective boundary condition statement, Eq (2.10), results for a_{1m} identified with the heat transfer coefficient, h, and a_{3m} set equal to a_{1m} multiplied by the reference temperature for heat exchange. Thus, the finite element algorithm accepts an arbitrarily varying, well-posed elliptic boundary condition statement on segments of all finite elements coincident with the global solution domain closure.

C. FINITE ELEMENT MATRIX GENERATION

Implementation of the solution algorithm into an operational computer code basically involves evaluation of the finite element matrices, Eq (2.20) and assembly and integration of Eq (2.21). For the simplex 1-, 2-, and 3-dimensional elements chosen, Figure 1, the use of natural coordinate systems is preferred, since evaluation of the required moment distributions, Eq (2.20), is particularly straightforward. A simplex natural coordinate is a (linear) function spanning the domain of a finite element, with the requirement that it vanish at all nodes of the domain except one where its value is unity. These functions are discussed in some detail in Reference 1, and are generalizations of the area coordinates of structural mechanics, extended to 1-, 2- and 3- dimensions, see Zienkiewicz (2).

The definitions of the natural coordinates for simplex functionals spanning 1-, 2- and 3- dimensional spaces are expressed in Table 1. The $\{L\}$ coordinate system is defined implicitly in terms of linear series approximations of the function involving the node point coordinates of the finite element. In each case, the first definition equation enforces the linear dependence of the natural system. The determinant of the matrix of coefficients modifying the definition of $\{L\}$ is algebraically related to the length, plane area, and volume of the 1-, 2- and 3-dimensional elements respectively. Evaluation of the finite element matrices, Eq (2.20) uniformly involves moment distributions over the domain of the finite element. The values taken for these moments are listed in Table 2 and are noted to involve only the exponent distribution of the elements of $\{L\}$. Note also the commutativity of the exponent distribution.

1. Planar Elements in Two-Dimensional Space

Evaluation of the finite element matrices in 2-dimensional space is straightforward, since moment generation is invariant under coordinate translation and rotation. The preferred orientation for the

TABLE 1
IMPLICIT DEFINITION OF LINEAR NATURAL
COORDINATE FUNCTIONS

Dimensions	Element	Nodes	Natural Coordinate Definition
1	Line	2	$\begin{bmatrix} 1 & 1 \\ x_1 & x_2 \end{bmatrix} \begin{Bmatrix} L_1 \\ L_2 \end{Bmatrix} = \begin{Bmatrix} 1 \\ x \end{Bmatrix}$
2	Triangle	3	$\begin{bmatrix} 1 & 1 & 1 \\ x_1 & x_2 & x_3 \\ y_1 & y_2 & y_3 \end{bmatrix} \begin{Bmatrix} L_1 \\ L_2 \\ L_3 \end{Bmatrix} = \begin{Bmatrix} 1 \\ x \\ y \end{Bmatrix}$
3	Tetrahedron	4	$\begin{bmatrix} 1 & 1 & 1 & 1 \\ x_1 & x_2 & x_3 & x_4 \\ y_1 & y_2 & y_3 & y_4 \\ z_1 & z_2 & z_3 & z_4 \end{bmatrix} \begin{Bmatrix} L_1 \\ L_2 \\ L_3 \\ L_4 \end{Bmatrix} = \begin{Bmatrix} 1 \\ x \\ y \\ z \end{Bmatrix}$

TABLE 2
INTEGRALS OF THE NATURAL COORDINATE FUNCTIONS

Dimensions	Integrals*
1	$\int_R L_1^{n_1} L_2^{n_2} dx = D \frac{n_1! n_2!}{(1+n_1+n_2)!}$
2	$\int_R L_1^{n_1} L_2^{n_2} L_3^{n_3} dx dy = D \frac{n_1! n_2! n_3!}{(2+n_1+n_2+n_3)!}$
3	$\int_R L_1^{n_1} L_2^{n_2} L_3^{n_3} L_4^{n_4} dx dy dz = D \frac{n_1! n_2! n_3! n_4!}{(3+n_1+n_2+n_3+n_4)!}$

* D = Determinant of coefficient matrix defining the natural coordinate system, see Table 1.

triangular element is in a local (unprimed) coordinate system, Figure 1, defined with respect to the global system by the tensor transformation law

$$x_j = \alpha_{ij} x'_i \quad (2.22)$$

The volume integration kernel, Eq (2.20), becomes

$$d\tau = t \, dx dy \quad (2.23)$$

where t is the thickness of the finite element. Surface integrals may be of two types involving integration over the plane area or along an edge of an element. In these cases, the surface integration kernels, $d\sigma$, respectively take the forms

$$d\sigma = \begin{cases} dx dy \\ t dx \end{cases} \quad (2.24)$$

where the x axis is always chosen to coincide with the side of the element coincident with the global domain closure segment. Except for the thermal conductivity matrix, $[K1]$, the evaluations are routine. Shown in the first column of Table 3 are the finite element matrices for all of Eq. (2.20), including the element dependent algebraic multiplier. A_m is the plane area of the finite element, and the boundary condition matrices are specified in terms of the convection coefficients h_m and T_{rm} and the specified heat flux F_m .

The thermal conductivity matrix requires some additional comment. Rewriting the second of Eq. 2.20 for 2-dimensional space, the $[K1]$ matrix becomes

$$[K1]_m \equiv \iint_{R_m} \{L\}_{,j} k_{ij}^m \{L\}_{,i} t \, dx dy \quad (2.25)$$

where k_{ij}^m is the element thermal conductivity tensor defined in the unprimed coordinate system. Since the elements of $\{L\}$ are linear, their first derivatives are constants and the integration reduces to evaluation of the plane area of the finite element. Performing the indicated summation operations on the repeated Latin subscripts, the $[K1]$ matrix takes the final form.

$$[K1]_m = A_m t_m \begin{bmatrix} L_{1,1} & L_{1,2} \\ L_{2,1} & L_{2,2} \\ L_{3,1} & L_{3,2} \end{bmatrix} \begin{bmatrix} k_{11}^m & k_{12}^m \\ k_{21}^m & k_{22}^m \end{bmatrix} \begin{bmatrix} L_{1,1} & L_{1,2} & L_{1,3} \\ L_{2,1} & L_{2,2} & L_{2,3} \end{bmatrix} \quad (2.26)$$

The k_{ij}^m tensor scalar components are obtained from the transformation definition and Eq (2.22) as

$$k_{ij}^m = \alpha_{pi} \alpha_{qj} k_{pq}^{m'} \quad (2.27)$$

Therefore, evaluation of $[K1]$ involves differentiation of the natural coordinate functions, Table 2, and the indicated matrix multiplications.

TABLE 3
FINITE ELEMENT MATRICES FOR THE ENERGY CONSERVATION EQUATION

Symbolic Matrix Eq. 2.20	Matrix Multiplier	Finite Element Matrices †	
		2-Dimensional Space	Axisymmetric Space *
$[C]_m$ (Specific Heat)	$\frac{\rho_m c_m A_m}{12}$	$t_m \begin{bmatrix} 2 & 1 & 1 \\ & 2 & 1 \\ & & 2 \end{bmatrix}$	$2\pi r_1 \begin{bmatrix} 2 & 1 & 1 \\ & 2 & 1 \\ & & 2 \end{bmatrix} + \frac{2\pi(r_2 - r_1)}{5} \begin{bmatrix} 2 & 2 & 1 \\ & 6 & 2 \\ & & 2 \end{bmatrix}$ $+ \frac{2\pi(r_3 - r_1)}{5} \begin{bmatrix} 2 & 1 & 2 \\ & 2 & 2 \\ & & 6 \end{bmatrix}$
$[K]_m$ (Thermal Conductivity)	A_m	$t_m \begin{bmatrix} L_{1,1} & L_{1,2} \\ L_{2,1} & L_{2,2} \\ L_{3,1} & L_{3,2} \end{bmatrix} \begin{bmatrix} k_{11} & k_{12} \\ k_{21} & k_{22} \end{bmatrix}$ $\begin{bmatrix} L_{1,1} & L_{2,1} & L_{3,1} \\ L_{1,2} & L_{2,2} & L_{3,2} \end{bmatrix}$	$\frac{2\pi(r_1 + r_2 + r_3)}{3}$ [same matrix as for 2-dimensional space]
$\{Y1\}_m$ (Int. Heat Generation)	$\frac{\rho_m \dot{Q}_m A_m}{3}$	$t_m \begin{Bmatrix} 1 \\ 1 \\ 1 \end{Bmatrix}$	$2\pi r_1 \begin{Bmatrix} 1 \\ 1 \\ 1 \end{Bmatrix} + \frac{2\pi}{4} \begin{Bmatrix} r_2 + r_3 - 2r_1 \\ 2r_2 + r_3 - 3r_1 \\ r_2 + 2r_3 - 3r_1 \end{Bmatrix}$
$[K21]_m$ (Conv. Boundary Condition)	$\frac{h_m x_2}{6}$	$t_m \begin{bmatrix} 2 & 1 \\ & 2 \end{bmatrix}$	$2\pi r_1 \begin{bmatrix} 2 & 1 \\ & 2 \end{bmatrix} + \frac{2\pi(r_2 - r_1)}{2} \begin{bmatrix} 1 & 1 \\ & 3 \end{bmatrix}$
$\{Y21\}_m$ (Conv. Boundary Condition)	$\frac{(h_m T_r - F_m) x_2}{2}$	$t_m \begin{Bmatrix} 1 \\ 1 \end{Bmatrix}$	$2\pi r_1 \begin{Bmatrix} 1 \\ 1 \end{Bmatrix} + \frac{2\pi(r_2 - r_1)}{3} \begin{Bmatrix} 1 \\ 2 \end{Bmatrix}$
$[K22]_m$ (Surface Convection)	$\frac{h_m A_m t_m}{12}$	$\begin{bmatrix} 2 & 1 & 1 \\ & 2 & 1 \\ & & 2 \end{bmatrix}$	† Symmetric matrices written in upper triangular form.
$\{Y22\}_m$ (Surface Convection)	$\frac{(h_m T_r - F_m) A_m t_m}{3}$	$\begin{Bmatrix} 1 \\ 1 \\ 1 \end{Bmatrix}$	* Node radial coordinates are in the global reference frame.

2. Planar Ring Elements in Axisymmetric Two-Dimensional Space

In this space, the matrix forms, Eq. (2.20), are invariant only under coordinate rotation, and require redefinition of the integration kernels. From the Jacobian of the transformation, Eq. (2.22), and differential geometry, the integration kernels in the unprimed coordinate system become

$$d\tau = 2\pi r' dx dy \quad (2.28)$$

$$d\sigma = 2\pi r' dl$$

where r' refers to the radial coordinate of points lying within the finite element expressed in the global coordinate system. From the definition of the natural coordinate system, r' becomes

$$r' = r'_1 + x_1 L_1 + x_2 L_2 + x_3 L_3 \quad (2.29)$$

Hence, for example, the specific heat matrix, Equation (2.20) takes the form

$$[C]_m \equiv \rho_m c_m \iint_{R_m} \begin{bmatrix} L_1^2 & L_1 L_2 & L_1 L_3 \\ & L_2^2 & L_2 L_3 \\ \text{(sym)} & & L_3^2 \end{bmatrix} (r'_1 + x_1 L_1 + x_2 L_2 + x_3 L_3) 2\pi dx dy \quad (2.30)$$

Performing the indicated integrations, Table 2, and collecting terms, the final form for $[C]_m$ becomes, in terms of the nodal radial coordinates (in the global system, but with primes deleted)

$$[C]_m = \frac{\rho_m c_m 2\pi r_1 A_m}{12} \left\{ \begin{bmatrix} 2 & 1 & 1 \\ & 2 & 1 \\ \text{(sym)} & & 2 \end{bmatrix} + \frac{\left(\frac{r_2}{r_1} - 1\right)}{5} \begin{bmatrix} 2 & 2 & 1 \\ & 6 & 2 \\ \text{(sym)} & & 2 \end{bmatrix} + \frac{\left(\frac{r_3}{r_1} - 1\right)}{5} \begin{bmatrix} 2 & 1 & 2 \\ & 2 & 2 \\ \text{(sym)} & & 6 \end{bmatrix} \right\} \quad (2.31)$$

As shown in Figure 1, node 1 is always the origin of the unprimed coordinate system and the numbering is counterclockwise. Note that the first matrix in Eq (2.31) is identical, to within 2π , to its 2-dimensional counterpart.

Evaluation of the remaining finite element matrices for axisymmetry, Eq (2.20), is similarly straightforward. The final forms are shown in the second column of Table 3. The thermal conductivity matrix, which is identical in 2-dimensional and axisymmetric space, is the sole matrix requiring numerical matrix multiplications.

III. HIGHLY STABLE EXPLICIT NUMERICAL INTEGRATION ALGORITHM

The explicit numerical solution of stable systems of differential equations with large Lipschitz constants creates serious integration step-size restrictions. This has motivated the derivation of explicit methods with increased ranges of stability, see for example References 3-6, as well as a proliferation of implicit methods. Restricting attention to explicit methods, techniques have become available for deriving integration methods that are optimum on the multiple bases of stability, accuracy, and required computing time(7). Methods are now available for evaluating any specified explicit integration algorithm for application to solution of a particular system of ordinary differential equations via use of a computer program specifically designed for this purpose(8). This work was recently specialized to optimally-stable, k-stage, one-step numerical integration methods(9), as well as a further restriction to 3-stage, one-step methods(10). The latter methods are distinctly applicable to the ordinary differential equation systems resulting from either finite element or finite difference discretizations of elliptic boundary value problems that are also initial value.

Briefly, a generalized family of numerical integration methods that are one-step, predictor-multiple-corrector formulas, are described by the equations

$$\begin{aligned}
 p_{n+1}^1 &= a_1^1 y_n + h b_1^1 y_n' \\
 p_{n+1}^2 &= a_1^2 y_n + h [b_1^2 p_{n+1}^1 + b_2^2 y_n'] \\
 &\vdots \\
 p_{n+1}^{k-1} &= a_1^{k-1} y_n + h [b_1^{k-1} p_{n+1}^{k-2} + b_2^{k-1} y_n'] \\
 y_{n+1} &= a_1^k y_n + h [b_1^k p_{n+1}^{k-1} + b_2^k y_n']
 \end{aligned} \tag{3.1}$$

A member of this family is called a "k-stage, one-step explicit integration method," and the special case $k=3$ is briefly summarized in the following discussion. The interested reader is referred to Reference 10 for details.

The computational structure displayed by Eq (3.1) is preferable to the popular k-stage, Runge-Kutta scheme, since it contains the potential to approximate the required solution at each stage, thereby rendering internal error control a natural adjunct to the process. As with Runge-Kutta methods, algorithms of the type Eq (3.1) are self-starting and easily programmed for digital computation. The 3-stage methods derived in Reference 10 enjoy optimally large stability ranges and minimal truncation error bounds. The most stable 3-stage methods are shown to be first-order, and their associated truncation errors may be computed with no requirement for additional derivative evaluations. Specialization of Eq (3.1) to 3-stage is straightforward, with y interpreted as the numerical approximation to the dependent variable, Y , which is the solution to Eq (3.2),

$$Y' \equiv \frac{dy}{dt} = f(Y, t) \quad (3.2)$$

In Eq (3.1) $h = t_{n+1} - t_n$, is the integration step size, and the a_1^k and b_1^k , $k = 1, 2, 3$, are real constants. The superscript prime denotes evaluation of the numerical approximation of the derivative expression, Eq (3.2), and $f(\)$ is a specified function of its argument. Note that Eq (2.21) is a vector equation with components in the form of Eq (3.2).

Two members belonging to the 3-stage family, Eq (3.1), have been derived for application to solution of large systems of ordinary differential equations. Both methods are first order accurate, i.e., their associated truncation error is of order h^2 , and they represent the most stable methods possible within the collection of first order accurate methods. The coefficients in Eq (3.1) for these two methods are listed in Table 4. Method 1 enjoys a large absolute stability interval, while Method 2 has an extended relative stability interval. That is, the application of Method 1 for solution of Eq (3.2) provides a propagated error which damps to zero for larger values of h than is possible by other methods. Similarly Method 2 creates a propagated error which damps monotonically for larger values of step size h . The real extent of the absolute and relative stability intervals of both integration methods is also shown in Table 4.

A feature enjoyed by the integration package built around Eq (3.1) is automatic error control based upon a user-specified parameter. The relative truncation error estimate magnitude for the subject integration methods can be written as ⁽¹⁰⁾

$$|RTE| = \frac{h}{\beta} \frac{|p_{n+1}' - y_n'|}{|y_{n+1}|} \quad (3.3)$$

The parameter, β , equals 3 and 6, respectively, for Methods 1 and 2. Eq (3.3) is utilized within the integration package to evaluate the relative truncation error associated with using the step size, h , to estimate the $n+1$ st value of the dependent variable. If the computed error is less than the user-supplied acceptable limit, the $n+1$ st estimate is accepted. At the same time, the integration algorithm will automatically increase h , by some fraction, before proceeding to the next time-step computation. In this fashion, the integration package consistently seeks to increase step-size and hence decrease solution computation time. If at some point the computed relative error exceeds the specified limit, the current predicted-corrected values for the dependent variable are discarded, a smaller step-size selected, and the operations of Eq (3.1) are repeated until an acceptable error is measured. These automatic features may be selectively overridden to march at a user-fixed step-size, or at a value of h not exceeding a specified value. The user may additionally select an initial step-size to start, or allow the program to compute an acceptable initial value.

TABLE 4
COEFFICIENTS IN FINITE DIFFERENCE INTEGRATION ALGORITHM,
EQ. 3.1, FOR TWO, ONE-STEP, THREE-STAGE METHODS

Coefficient	Method 1	Method 2
a_1^1	1.0000	1.0000
a_1^2	1.0000	1.0000
a_1^3	1.0000	1.0000
b_1^1	0.1549	0.2877
b_1^2	0.2711	0.2920
b_2^2	0.7289	0.7080
b_1^3	0.1667	0.3334
b_2^3	0.8333	0.6666

Absolute Stability Interval	$(-15.997, 0]$	$(-8.765, 0]$
Relative Stability Interval	$(-1.245, 0]$	$(-7.998, 0]$

IV. FINITE ELEMENT COMPUTER PROGRAM

The general purpose finite element computer program COMOC (Computational Continuum Mechanics) is coded completely in terms of generalized, nondimensional independent and dependent variables. In addition to producing the results using the Thermal Analysis Variant of COMOC, it has been exercised for problems in hydrodynamics⁽¹¹⁾, three-dimensional boundary layer flow⁽¹²⁾, and the compressible Navier-Stokes equations⁽¹³⁾. The program is briefly described as follows; the interested reader may obtain details in Reference 14.

The COMOC program consists of four basic Modules, as illustrated in Figure 2. In INPUT, the desired discretization is formed by user specification of the plane global coordinates of the nodes of each triangular-shaped finite element. The node numbering sequence is completely arbitrary, as is the selection of a particular discretization, and both may be chosen for output convenience. In particular, nodes may first be placed where output information is desired. The remainder of the solution domain is then discretized to avoid finite elements with aspect ratios greater than about 70:1. The closure of the solution domain is recognized by the program as the counterclockwise connection of a specified sequence of N nodes.

The element definition is obtained by identifying the three vertex nodes, the thermophysical properties material number, and thickness of each finite element. The non-vanishing boundary condition coefficients, a_{im} , Eq (2.20) are also included on the element cards as is internal heat generation. The input phase is completed by reading the material properties tables, various control parameters of the integration algorithm of Module 3, initial conditions information, and the desired output control parameters.

The next two Modules, Figure 2, are basically DO loops on the finite elements of the discretization. In the GEOMETRY Module, the finite element matrices, Eq (2.20), are formed. The INTEGRATION Module embodies the numerical solution algorithm for both algebraic and ordinary differential equation systems; the Thermal Analysis Variant uses only the latter. The basic element operation is formation of Eq (2.19), at a given time station, and assembly of the element matrices into the global representation, Eq (2.21). At user-selected points, the OUTPUT Module is called to record the present values of the elements of the temperature vector $\{\theta(t)\}$ and other desired parameters.

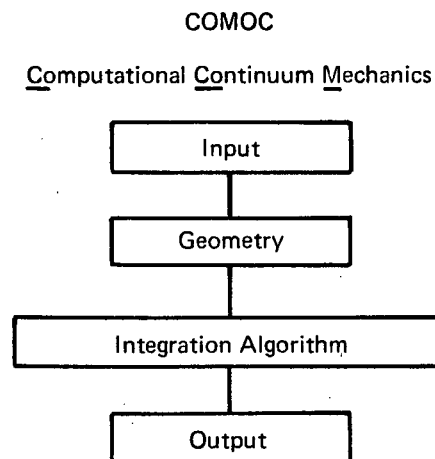


Figure 2. COMOC Computer Program Organization

V. NUMERICAL RESULTS

An extensive literature has developed over recent years devoted to experimentation with finite element methods for problems in heat conduction and other linear field problems. Zienkiewicz and Cheung (15) published an early contribution detailing a finite element solution algorithm for a linear Poisson equation, and illustrated its usefulness for the steady-state heat conduction problem. Shortly thereafter, Wilson and Nickell (16), employing a pseudo-variational principle after Biot (17) and Gurtin (18), established a finite element algorithm for transient heat conduction in linear continua. Baker (19) generalized the theory to include temperature-dependent thermophysical properties. Concurrently, Finlayson and Scriven (20, 21) concluded that pseudo-variational principles were generally not required, and that comparable algorithm forms resulted from select use of specific criteria within MWR. The 1969 ASME Winter Annual Meeting Heat Transfer Session (22-27) included many finite element contributions. Mason, et.al. (28, 29) employed structural computer codes for thermoelastic analysis of laser mirror systems. The use of isoparametric finite elements has been suggested by Zienkiewicz and Parekh (30) for transient heat conduction problems.

It is quite logical that these referenced authors, whose predominant residence is in the structural mechanics community, would contribute to early developments, since they possessed operational finite element computer programs that could be adapted for experimentation on heat conduction problems by redefinition of dependent variables and continuum properties. These encouraging initial numerical results provided the impetus to consider building a computer system tailored to the generalized field problem class, and several are now in progress, including the NASTRAN (NASA Structural Analysis) system. This is the concept behind COMOC as well. The Thermal Analysis Variant of this computer program has been extensively exercised to validate the mathematical soundness of the generalized theory, to evaluate the accuracy and convergence character of computed solutions, to prove the significant speed with which practical problem solutions can be obtained, and to illustrate the great versatility of the generalized finite element computer program system. COMOC has produced the favorable assessments that are discussed in this section.

A. ACCURACY AND CONVERGENCE WITH DISCRETIZATION

Since no rigorous variational statement exists for the general quasilinear elliptic-initial value problem for which the finite element solution algorithm was derived, a numerical evaluation of accuracy of the computed solutions, and convergence toward the correct solution with finer discretization, is required. The problem selected was external transient convective heat exchange between a medium at constant temperature and a thick axisymmetric cylinder with temperature independent thermophysical properties. A truncated series solution (31), valid for small solution time and for locations near the exterior cylinder surface, was used as the comparison analytic solution.

The accuracy of solution was found to be a function of discretization as well as the manner selected for assembly of the global specific heat capacity matrix, $[C]$. It is recalled that the inverse of $[C]$ is required to render the finite element solution algorithm in standard form, Eq (2.21), for integration by explicit techniques. Employing the rigorous definition for specific heat capacity matrix, $[C]_m$, Eq (2.20) at the element level yields a global $[C]$ which is a sparse symmetric matrix banded about the main diagonal. The bandwidth is a function of discretization, and the matrix may be inverted by classical algebraic means, or essentially evaluated using equation solver techniques, e.g., banded Cholesky. The $[C]$ matrix may be rendered diagonal, and the inversion operation trivial, by condensing the specific heat capacity of each finite element at the node points. Such an operation, commonplace in some structural dynamics problems wherein lumped mass matrices replace the consistent formulation, is accomplished by adding rowwise

the matrix elements of each $[C]_m$ within a finite element, and placing the nonvanishing coefficient on the diagonal. From Table 3, this operation is noted to equally distribute the element heat capacity at the nodes for two-dimensional problems; in axisymmetry, the result of condensing is dependent upon the particular element location and geometry.

Both of these options have been evaluated by COMOC for several discretizations of the thick cylinder problem. An illustration of the 32 finite element discretization of the cylinder cross-section is shown in Figure 3, as well as the various vanishing gradient and convection boundary conditions. Discretizations employing elements spanning double and half the radial domain (16 and 64 finite elements) of the 32 element case were also evaluated. The thermophysical material properties were that of Type 304 stainless steel, and the convective heat transfer coefficient and exchange temperature were 34.6 w/m^2 (20 Btu/hr ft^2) and 311°K (100°F) respectively. The initial cylinder temperature was uniformly 255°K (0°F) for all tests.

Shown in Table 5 is the comparison between the exact solution and the results of computations by COMOC, for the transient temperature distribution at and near the surface of the cylinder and within the essential accuracy bounds of the truncated series solution. The results in the first three COMOC columns, for 16, 32 and 64 element discretizations using the condensed $[C]$ form, show smooth convergence, generally from below, to the correct solution. The same general behavior is noted in the last columns of Table 5 for the 16 and 32 element cases using the full $[C]$ form; however, explicit violations of the second law of thermodynamics are noted, in both cases, for nodes interior to the surface. At these locations, depression of temperature below the uniform 255°K (0°F) initial value for a positive heat flux into the solution domain is observed. Similar results have occurred for other discretizations and different boundary conditions and thermophysical properties. In general, a larger applied flux and/or smaller thermal conductivity render the temperature depressions more severe (up to -5.0°K (-10°F) for the cylinder made from an insulator like asbestos). A finer discretization has always improved this adverse phenomena.

The accuracy comparison between the full and condensed specific heat matrix forms is shown in Figure 4. For full $[C]$, the finite element solution agrees well with the analytic solution at the exterior wall, $r = 0.61 \text{ meters}$ (2.0 ft). The extent of the interior temperature depressions is evident. The 32-element, condensed $[C]$ solution enjoys accuracy comparable to the 16-element full $[C]$ solution at the wall, and is uniformly more accurate in the interior. The 16-element condensed $[C]$ solution is considerably poorer than either discussed solution.

These results are in essential agreement with the experience using consistent and lumped mass matrix solutions in structural dynamics, as well as the cursory results of Reference 16. The consistent (or full) formulation can provide more accurate solutions using coarse discretizations. Both full and condensed solutions converge with discretization; for this particular sample case, a doubling of the discretization and moving to the condensed form provided a uniformly comparable or more accurate solution.

These discussed accuracy and convergence results were obtained for the highly stable integration algorithm package (QKNINT, Quick Numerical Integrator) operating well with its stability bounds, since the allowed step-size was constrained by requested output. To determine the stability character, and resultant computer CPU execution times for the different $[C]$ matrix options, as well as illustrating the automatic step-size and error control features of QKNINT, the convective loading to the 32 element thick cylinder was increased 20-fold and the thermal conductivity increased by a factor of 4 to produce the required test problem. Figure 5 shows comparison surface temperature computations, and the automatically determined integration intervals used by QKNINT, Methods 1 and 2 in obtaining the plotted transient solutions. Using a value of $\epsilon = 0.001$ for the QKNINT error control parameter, the solution accuracy for Methods 1 and 2 for the full $[C]$ matrix form is essentially identical. However, as shown,

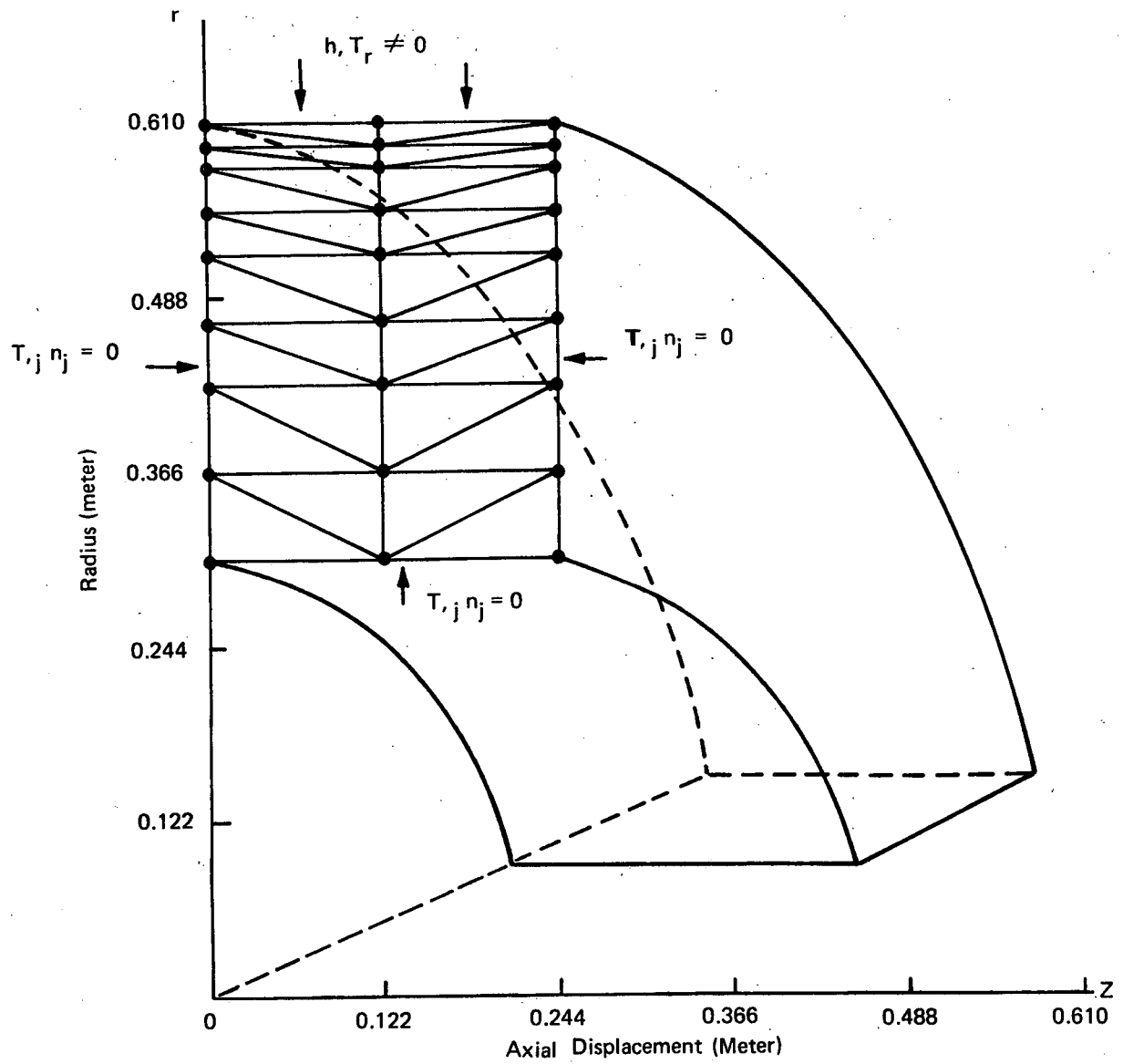


Figure 3. Discretization of Thick Axisymmetric Cylinder into Thirty-two Triangular Cross-Section Ring Finite Elements

TABLE 5
TRANSIENT TEMPERATURE DISTRIBUTIONS IN
THICK AXISYMMETRIC CYLINDER

Node Radius (m)	Solution Time (sec)	Temperature °K Series Solution (31)	COMOC Computed Temperature (°K)				
			Condensed C Matrix			Full C Matrix	
			16 Element	32 Element	64 Element	16 Element	32 Element
0.61	0.0	255.38	255.38	255.38	255.38	255.38	255.38
	79.2	259.92	258.49	259.58	259.93	259.51	259.85
	158.0	261.63	260.65	261.50	261.68	261.53	261.66
	237.6	262.87	262.15	262.82	262.97	262.84	262.94
	316.8	263.88	263.30	263.87	264.02	263.84	263.98
	396.0	264.73	264.20	264.75	264.90	264.57	264.87
	475.2	265.47	265.20	265.53	265.69	265.31	265.66
0.58	0.0	255.38	255.38	255.38	255.38	255.38	255.38
	79.2	255.54	255.53	255.52	255.49	255.12	255.39
	158.0	256.14	255.89	255.99	256.07	255.63	255.97
	237.6	256.86	256.41	256.65	256.81	256.42	256.73
	316.8	257.58	256.97	257.36	257.54	257.14	257.49
	396.0	258.27	257.60	258.07	258.27	257.95	258.21
	475.2	258.92	258.21	258.74	258.94	258.61	258.89
	554.4	259.53	258.82	259.37	259.58	259.43	259.53
	792.0	261.16	260.45	261.10	261.32	261.07	261.25
	1029.6	262.53	262.18	262.58	262.84	262.72	262.72
0.52	0.0	255.38	255.38	255.38	255.38	255.38	255.38
	158.0	255.38	255.39	255.38	255.38	255.30	255.36
	237.6	255.39	255.41	255.39	255.38	255.09	255.34
	316.8	255.40	255.45	255.41	255.40	254.88	255.32
	396.0	255.44	255.50	255.45	255.44	254.98	255.33
	475.2	255.51	255.56	255.51	255.50	255.02	255.37
	554.4	255.60	255.64	255.60	255.59	255.07	255.46
	792.0	256.00	256.02	255.96	255.99	255.41	255.85
	1029.6	256.52	256.34	256.46	256.53	255.99	256.38

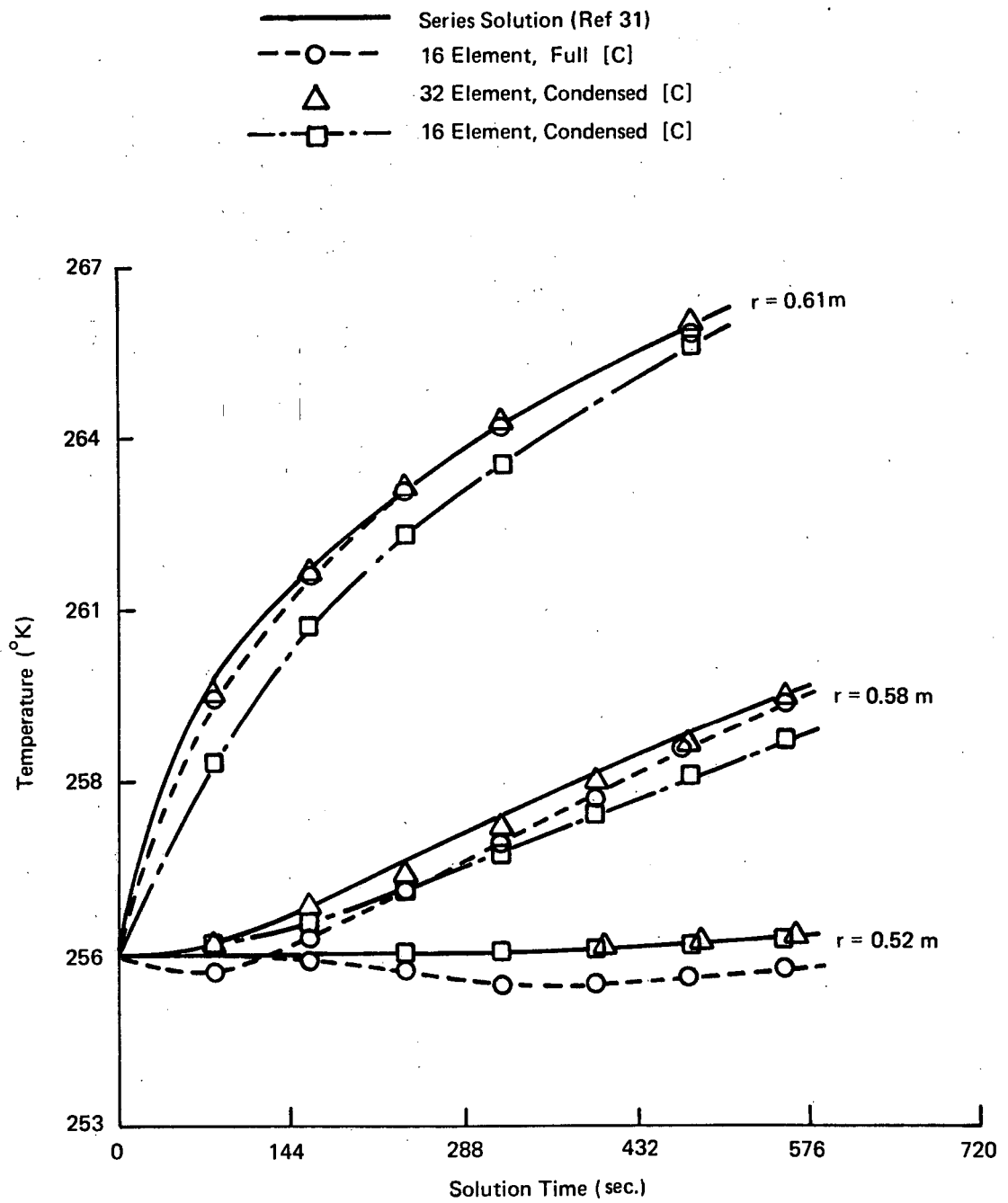


Figure 4. Accuracy Comparison of Computed Transient Temperature Distributions in Thick Axisymmetric Cylinder As Function of [C] Form and Discretization

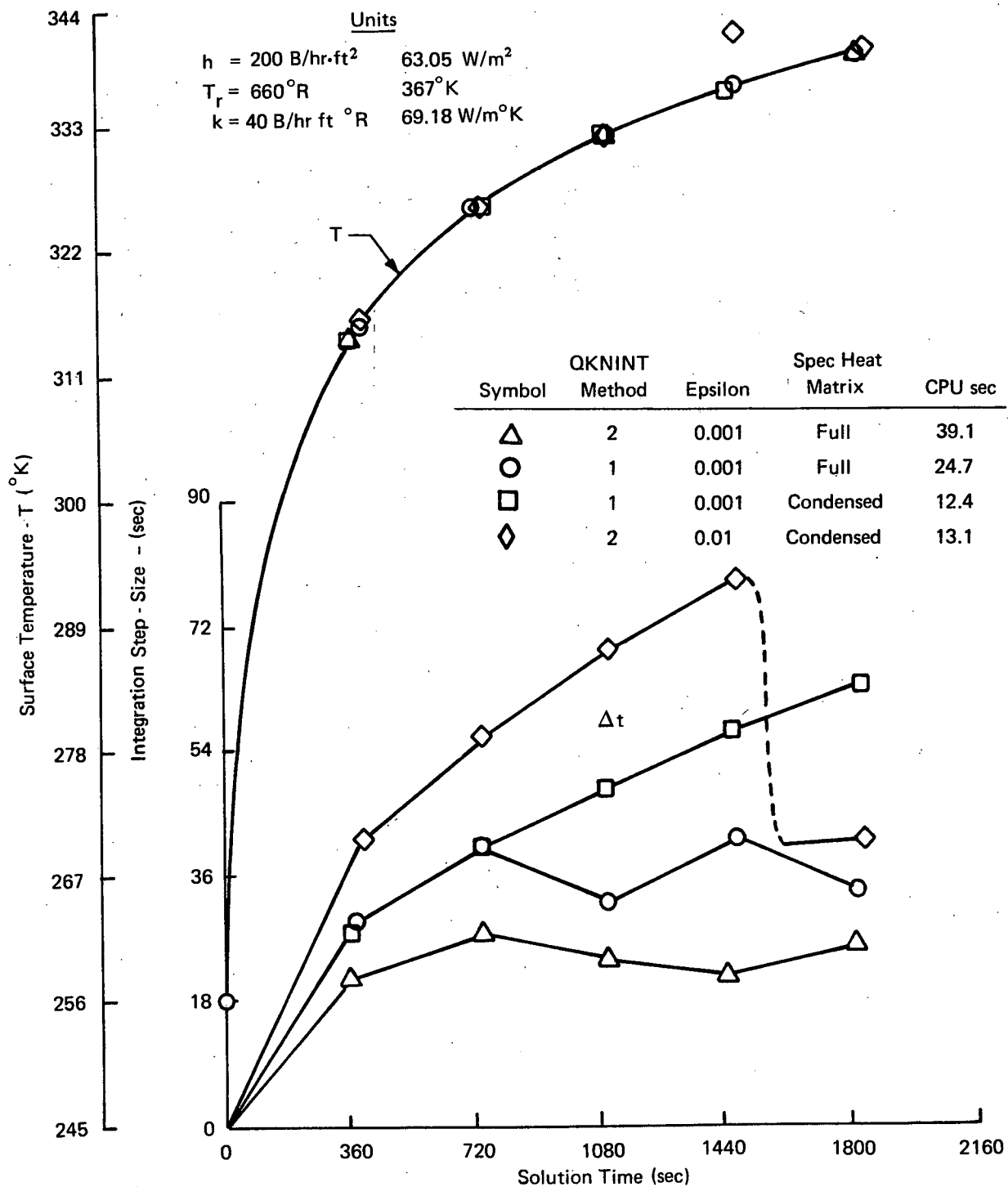


Figure 5. Comparison of Surface Temperature and Integration Step-Size for Different Integration Methods and Matrix Forms For Thirty-Two Element Cylinder Discretization

Method 2 marched at a considerably smaller integration step-size (as expected, see Table 4), and consequently took 50% additional CPU time to achieve the solution end point. Switching to the condensed [C] matrix, $\epsilon = 0.001$, maintained comparable solution accuracy, and achieved the solution in half the CPU time of the full [C] solution. This economy results directly from the increased stability of the condensed [C] differential equation system, Eq (2.21), as evidenced by the significantly larger step sizes used by QKNINT for the same Method. This speed factor, coupled with the accuracy determination previously discussed, indicates that use of condensed [C] is uniformly preferable to full [C] for practical problems.

Decreasing the accuracy parameter to $\epsilon = 0.01$ for Method 2, and using the condensed [C] form, produced the illustrated results which were obtained on the fringe of instability. Note the surface temperature excursion at $t = 1440$ sec. (0.4 hr), the immediate reduction in integration step size, and the return to an accurate solution. This is a completely automatic operation within QKNINT and requires no user insight or control, other than specification of the error parameter.

The results of these as well as many other tests indicate that specifying $\epsilon = 0.01$ will in generally produce the most speedy solutions while maintaining generally adequate accuracy. However, on rare occasions, $\epsilon = 0.01$ has allowed errors to propagate beyond return, with the resultant solution diverging to nonsense. Setting $\epsilon = 0.001$ has uniformly resulted in smooth stable solution behavior, usually for somewhat increased solution CPU times. The specific choice of the option belongs to the user.

The results shown in Figure 6 additionally illustrate the automatic features of QKNINT, as well as indicating the attainment of smooth, well behaved solutions for $\epsilon = 0.01$. Shown are transient surface temperature histories for the thick cylinder problem with different thermal conductivities. The thermal conductivity matrix, the counterpart of the stiffness matrix in elasticity, forms the major contribution to the Jacobian of the solution differential equation system, Eq (2.21). Hence, the stability character is strongly influenced by changes in thermal conductivity. QKNINT automatically determined a lower-bound estimate to the maximum allowable initial integration step size, HMIN, as a function of k as tabulated. It similarly obtained a lower-bound estimate of the maximum allowable step-size, HMAX, as a function of the generated solution. Note that the $k = 69.2$ w/m²°K (40 Btu/hr ft²°R) solution found the relatively largest HMIN and smallest HMAX; as a consequence, it required the largest CPU execution time. This illustrates the important feature of the QKNINT package of completely automatic operation, and a built-in capability to tailor the solution constraints to the particular differential equation system being solved, as a function of the error control parameter epsilon.

B. ACCURACY AND SOLUTION SPEED FOR A PRACTICAL ENGINEERING PROBLEM

The problem selected for illustrating the engineering usefulness of COMOC is the pulsed firing of a small, axisymmetric thrust-vector-control rocket motor. Such devices, commonplace in many aerospace, missile and spacecraft systems, are subjected to severe cyclic thermal loading from the contained combustion of propellants. Hence, very large (radial) temperature gradients can be induced, and the structural integrity of the nozzle throat is of fundamental importance. Therefore, accuracy of the computed solution especially in the throat region, is critically important.

The assessment of computational accuracy was made by comparing COMOC solutions to those generated by an independent, state-of-the-art, multi-dimensional heat transfer computer program. The theoretical foundation of the solution algorithm for this comparison program is the "electric analog" to heat conduction, wherein heat capacities are assigned to nodes, and equivalent thermal "resistances" between nodes are established based upon the material thermophysical properties and the node distribution. An entirely equivalent theoretical basis exists within the MWR finite element theory established in Section

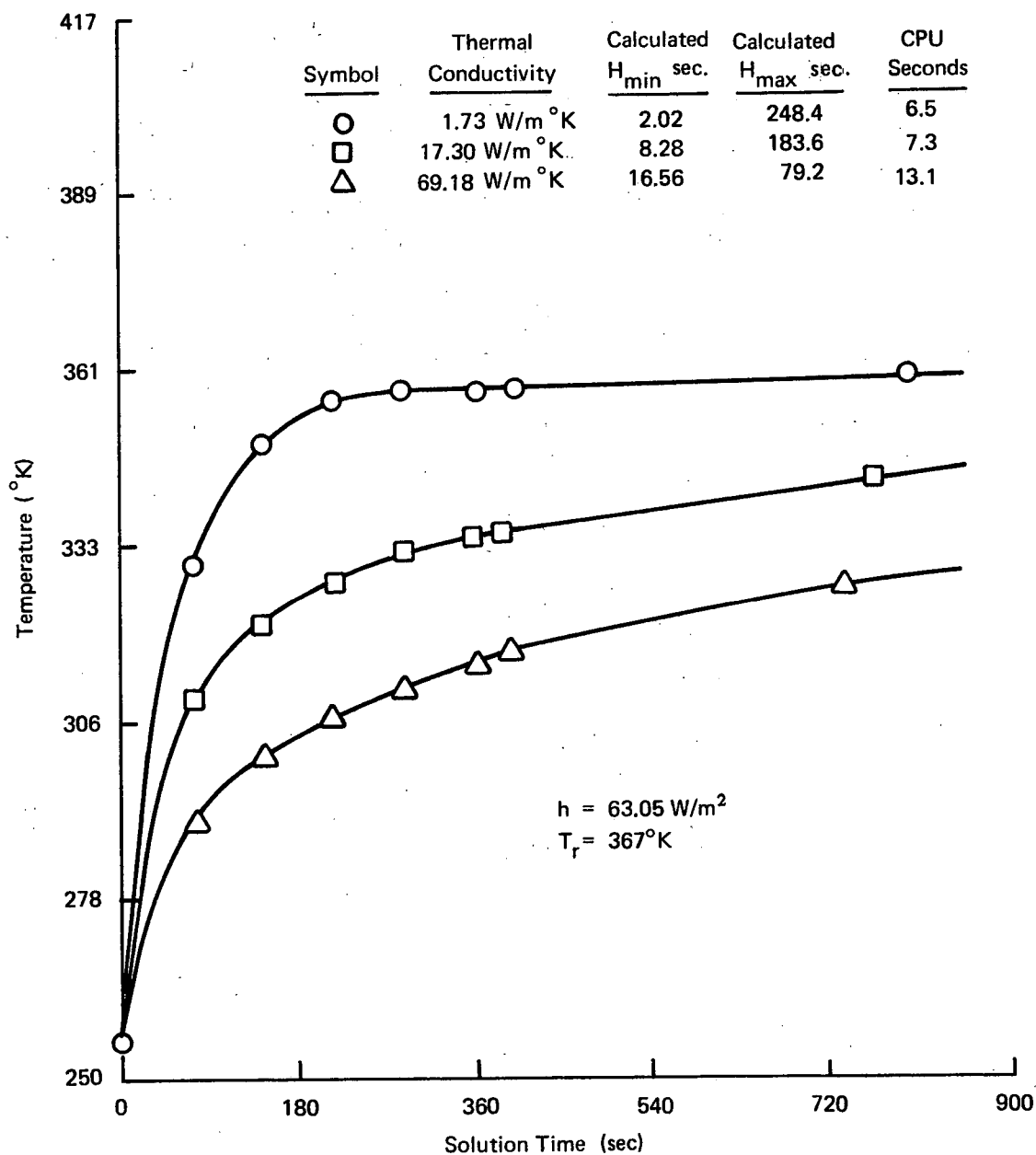


Figure 6. Transient Surface Temperature of Thick Axisymmetric Cylinder as Function of Thermal Conductivity, Epsilon = 0.01, Method 2, Condensed Matrix

II, which leads to an apparent "finite difference" formulation. (32) To form this basis, assume that the temperature approximation function within a given solution element, T_m^* , Eq (2.18), can be represented by a spatially uniform temperature located at coordinates (ξ_i) within the element, i.e., $\theta_m(\xi_i, t)$. Employing a scalar constant for the weighting function, W_k , Eq (2.16) in conjunction with $\theta_m(\xi_i, t)$ yields an algorithm form identical in appearance to Eq (2.21). However, to complete the algebra, and since $\theta_m(\xi_i, t)$ is spatially constant, a finite difference approach must be used to evaluate the element thermal conductivity matrix, $[K]_m$, Eq (2.20). Typically, a first order difference is used, with the assumption that the coordinates (ξ_i) are identical with the element geometric centroid $(\bar{\xi}_i)$ for interior elements, and that elements at a convention boundary are half-thickness and (ξ_i) lies at the surface centroid.

Figure 7 is an illustration of the subject rocket motor. The overall length of the device is about 0.15 meter (6 inches); the downstream half was selected as the computational problem domain, spanning from the center of the combustion chamber through the terminus of the nozzle. Also shown in Figure 7 is the 104 finite element discretization used for the majority of COMOC computations. This discretization was formed from the parent "finite difference" discretization, which employed quadrilateral shaped solution domains. (Note the specification of half-width quadrilaterals at the internal and external cylindrical convection surfaces.) Each of these domains were bisected to form the triangular element shape required for the finite element solution. Hence, the discretizations were approximately uniform for the comparison methods. However, as a consequence of the difference between the formalisms, the 52 finite difference quadrilaterals yielded 52 node point temperatures for computation, while the 104 finite elements yielded 70 node temperatures for integration.

The boundary condition specifications were vanishing normal temperature gradients at the left and right ends of the solution domain (see Figure 7) and an adiabatic outer surface. In actual practice, the inner surface of the motor is loaded by radiation from the contained hot gas. While this is capable of solution, Eq (2.11), the considerable difference in computed surface temperatures between the methods, to be discussed, would deleteriously affect the desired comparisons. Hence, for computational purposes, the nozzle was loaded convectively by a uniform internal gas temperature of 3611°K (6040°F) and the convection heat transfer coefficient distribution over the surface of interior elements illustrated in Figure 7. The maximum energy flux, occurring at the nozzle throat, was about $9.5 \times 10^5 \text{ w/m}^2$ ($3 \times 10^6 \text{ Btu/hr ft}^2$), and this produced throat temperatures at the end of a 10-second firing that were comparable with the results of laboratory experimentation. The rocket material was selected as a stainless steel, the thermo-physical properties of which vary approximately by a factor of two for the temperature range encountered during the ten-second firing.

Illustrated in Figure 8 are the comparisons between the COMOC computed and "finite difference" program results for axial temperature distributions on and near the interior and exterior surfaces of the rocket motor after a 10-second firing. The node rows for which the COMOC results are plotted are shown in Figure 7. The "finite difference" comparison solutions, from theoretical considerations and near equilibrium, must be bounded by the respective finite element solution; in addition, they should lie closer to the extreme COMOC computed temperatures. The comparison results confirm theoretical predictions excellently at both rocket surfaces. The approach to actual surface temperature by the "finite difference" solution is poorest where the temperature levels and gradients (hence departure from equilibrium) are largest. At the throat, the COMOC results are 111°K (200° R) higher, and the "finite difference" solution is effectively the mean of the actual temperature distribution within the computational cell. The excursion of the "finite difference" solution beyond the finite element bound, at the extreme downstream end of the rocket, is probably associated with difficulty in establishing the correct approximation to the vanishing gradient boundary condition for the skewed quadrilateral zones employed there (Ref. Figure 7). The correct bounded behavior occurs at the left end for a similar boundary condition and regular quadrilateral cells.

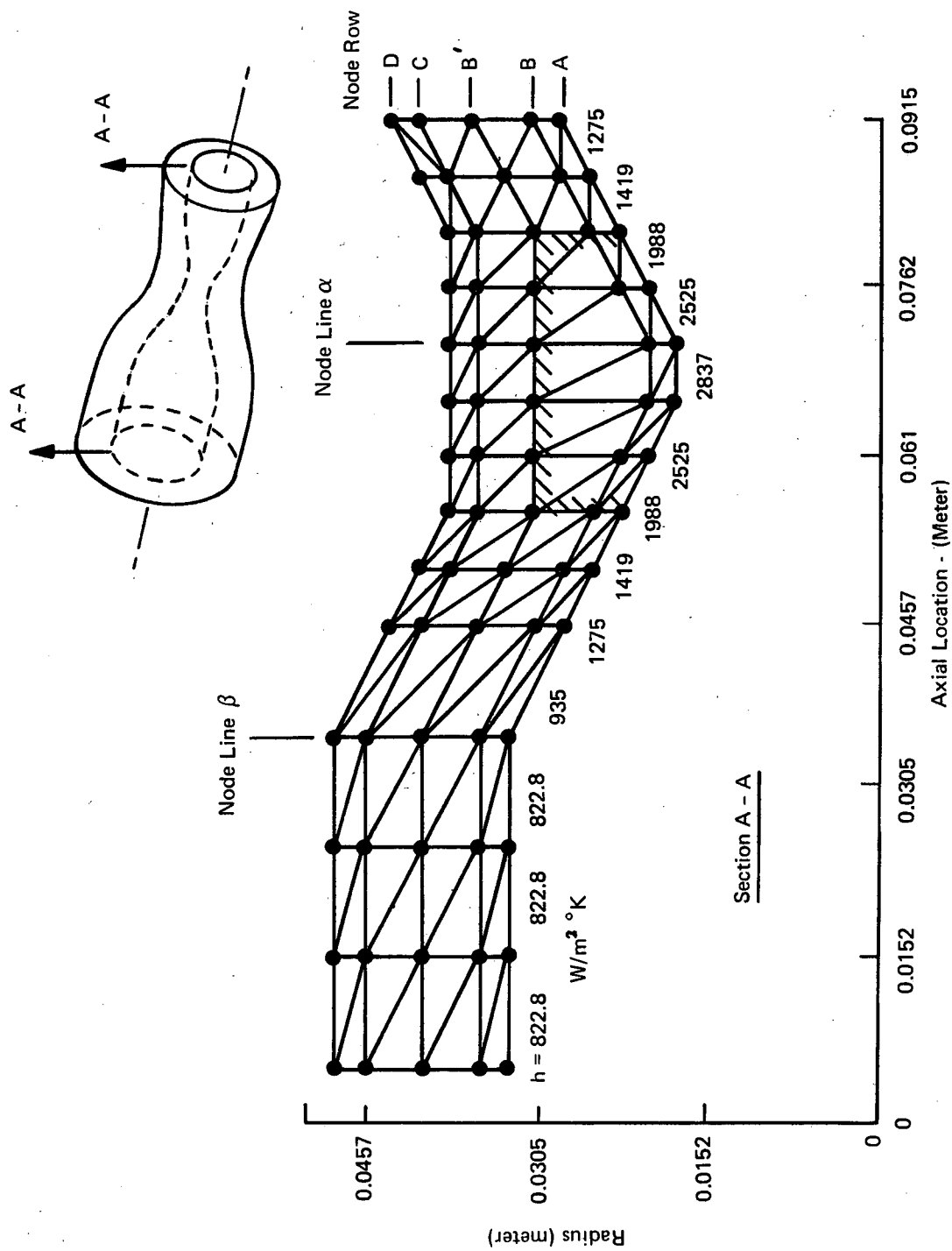


Figure 7. Discretization of Axisymmetric Rocket Motor Into 104 Triangular Cross-Section Ring Finite Elements

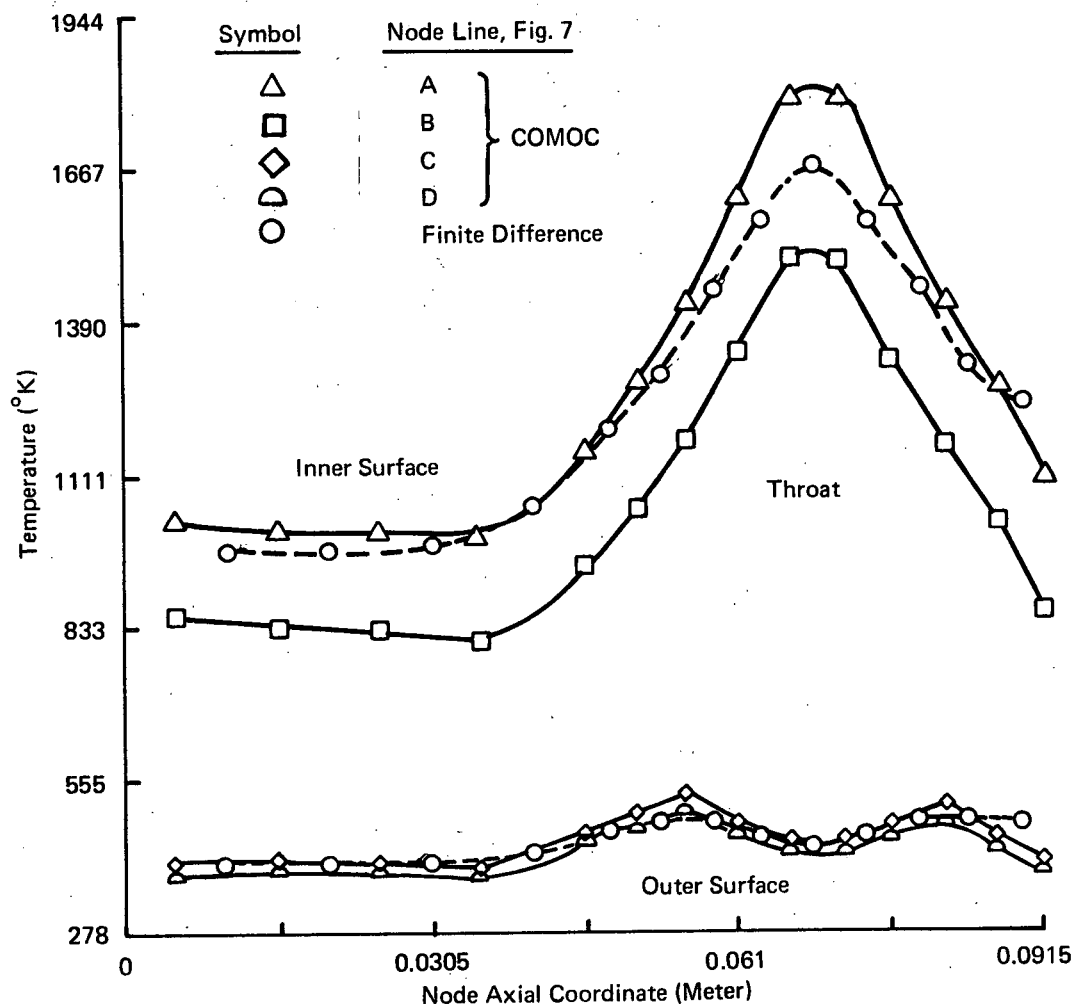


Figure 8. Comparison of Computed Axial Temperature Distributions After Ten Second Firing of Rocket Motor

Figure 9 illustrates the comparison between the transient temperature distribution at the nozzle throat, and at the exterior wall along Node Line α , Figure 7, as computed by COMOC and the comparison computer program. Along the exterior surface, the finite difference solution is continually bounded by the finite element solution. The behavior at the nozzle throat is essentially identical except for a modest over-shoot in the neighborhood of $t = \sim 3$ seconds (0.001 hours). This excursion probably results from the gross underprediction of surface temperature by the finite difference program during the initial time of firing (over 333°K (600°R) at time equals one second). The most significant departure from equilibrium occurs simultaneously with this underprediction. The assumption that the temperature node location (ξ_i) of the finite difference analogy occurs at the surface of half-width quadrilateral elements during rapid transients is thus observed to be a poor approximation.

The results of these comparison studies using the two different computer programs for the identical problem have verified the theoretical predictions concerning the two different solution formalisms. They show the significant improvement in accuracy that can result from application of finite element techniques to problems involving severe transient phenomena. In combination with the accuracy and convergence results for the thick cylinder problem, the mathematical theory and computational practice for the finite element solution algorithm appears well founded and validated.

Extensive experimentation has been conducted on the rocket motor problem, using the COMOC computer program to assess solution speed and accuracy. Figure 10 shows an actual COMOC output page showing the temperature (in common units) in the nozzle, after one second of firing, in a format that is geometrically similar to the actual rocket motor geometry. The boundary of the motor has been sketched in, as well as the approximate location of the 333°K , 611°K (600°R , 1100°R) isotherms. Such user-oriented routines greatly enhance the readability and practical usefulness of computer output; these routines may be easily prepared by the engineer using COMOC, and can present geometrically similar data outputs for any arbitrarily irregular discretization. The user may output the temperature derivative vector, $\{\theta(t)\}'$, Eq (2.21), as well as is illustrated. A very quick glance at this array identifies locations where the solution field is most rapidly changing.

The 104 finite element discretization of the rocket motor is rather coarse. To check accuracy of COMOC, a 538 finite element discretization, shown in Figure 11, was established by quartering each finite element of the original discretization and adding additional elements in the thick section behind the nozzle throat. Shown in Figure 12 is the COMOC computed temperature distribution within the motor after one-second of firing. The rocket boundary has been sketched in, as well as the 333°K , 611°K (600°R , 1100°R) isotherms for comparison to Figure 10. Note also how the output routine has been altered to encompass the larger problem output.

Assessment of the solution accuracy for the 104 element case, made by comparing Figures 10 and 12, shows that the coarser discretization tended to uniformly underpredict temperature at any given location, in agreement with the thick cylinder discretization results. Shown in Figure 13 are the computed radial temperature distributions at the nozzle throat and through the combustion chamber wall (Node Lines α and β , Figure 7, respectively). At the nozzle, the 104-element case predictions are 111°K - 167°K (200 - 300°R) lower, although the computed temperature gradients are essentially identical. The 538-element case has added significant temperature definition to the region interior of the throat, Node Line α . Very little difference in temperature predictions are noted through the combustion chamber wall, Node Line β .

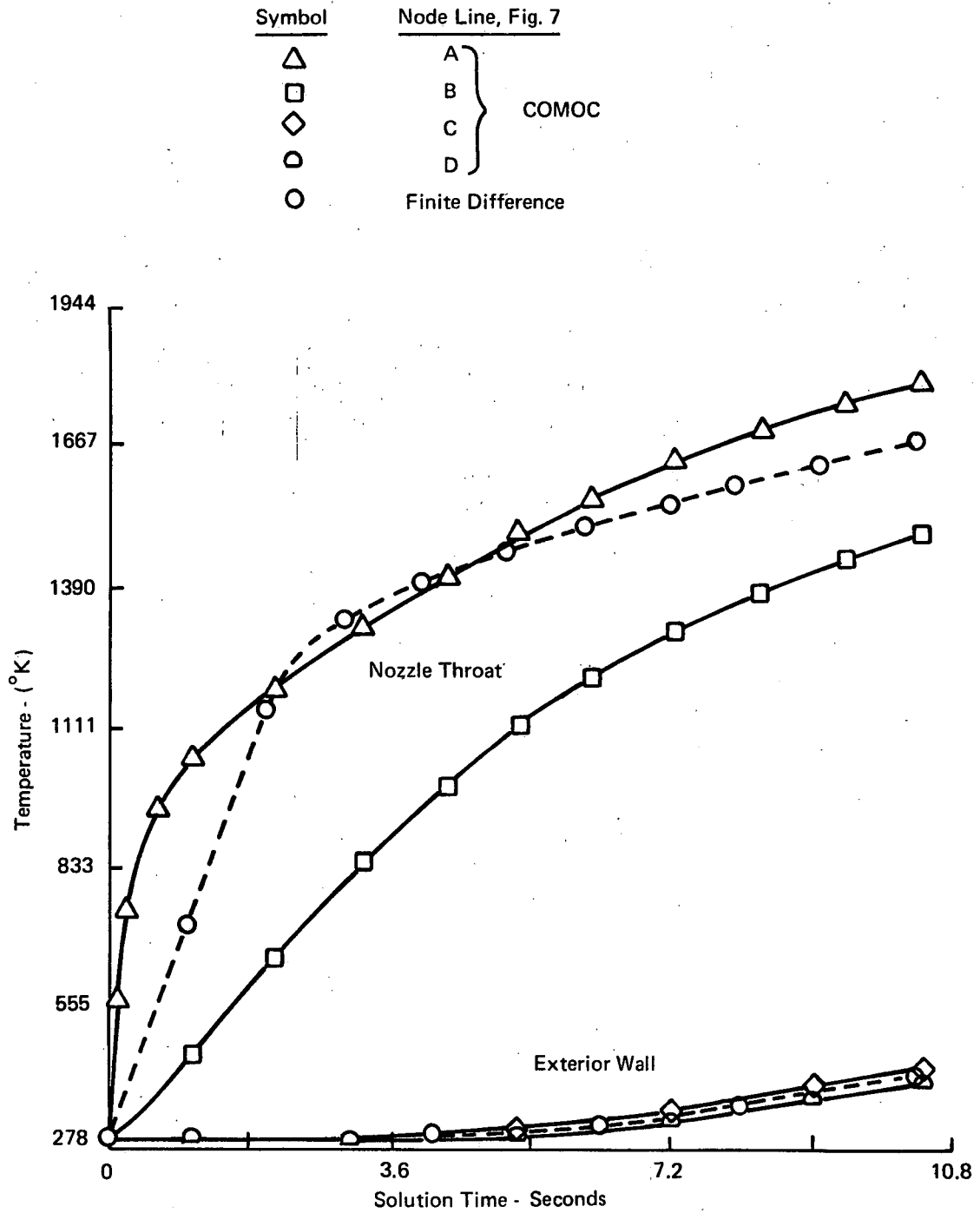


Figure 9. Comparison of Computed Transient Temperature Distribution at Nozzle Throat of Rocket Motor During Ten Second Firing

CASE 3-1, ROCKET NOZZLE , DIAGONAL C-MATRIX, QKNUMN FACTOR=4.0
QKNINT, KEY=1, EPS=0.01 , KPRINT=1 DELP=.000288, HMIN=0., TF=.00288
K=10.0, HC=VAR , TREF=6460., ALC=0.1

TIME = 0.000 288 HOURS CURRENT INTEGRATION STEP SIZE = 0.80000E-04 HOURS

[illegible][illegible][illegible]

QKNINT
CUMULATIVE NUMBER OF TIMES STEP SIZE WAS DECREASED = 1 AND INCREASED = 8

Figure 10. Computed Temperature Distribution within Rocket Motor After One Second Firing, 104 Finite Element Discretization

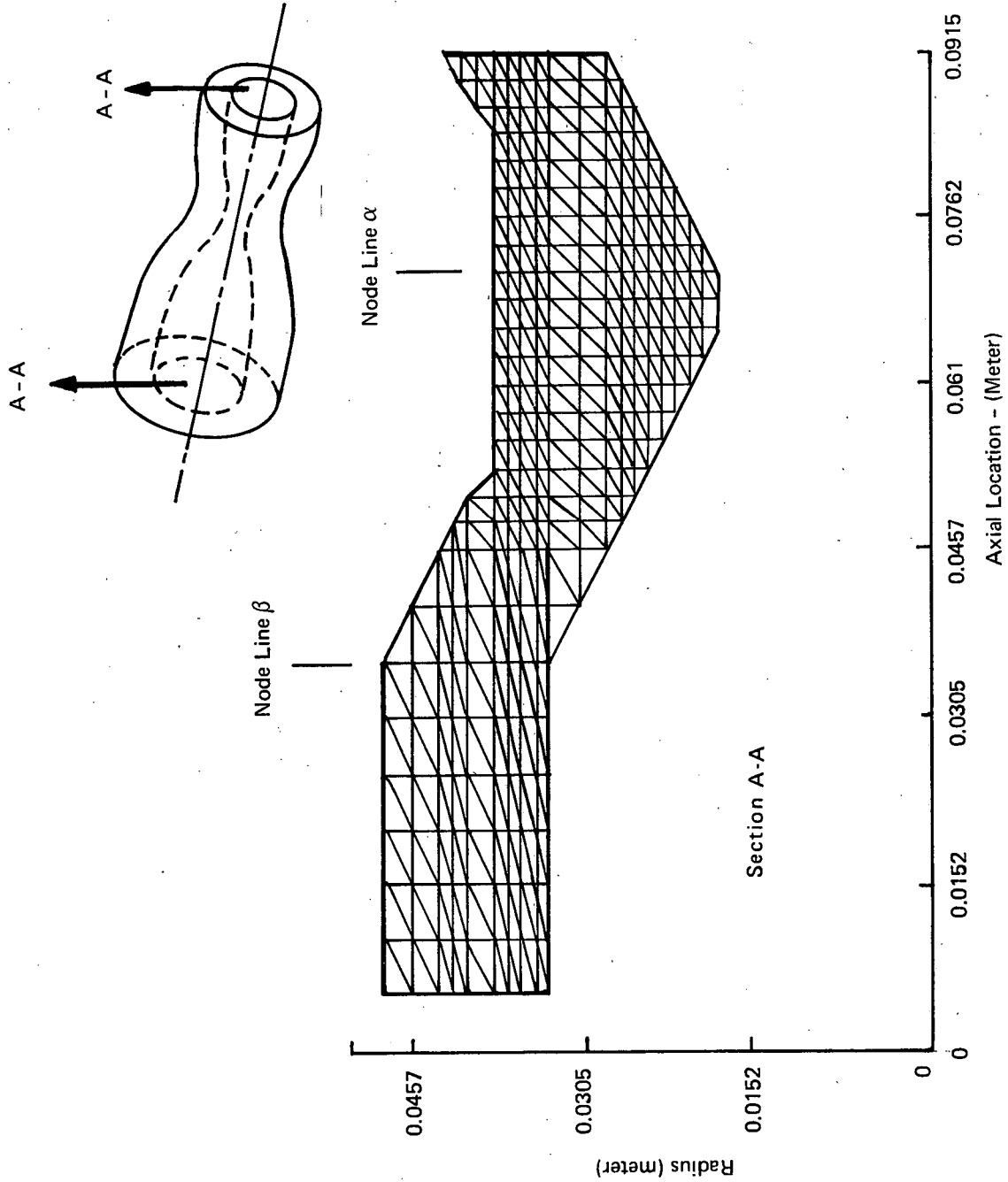


Figure 11. Discretization of Axisymmetric Rocket Motor Into 538 Triangular Cross-Section Ring Finite Elements

C. G. M. O. C.
COMPUTATIONAL CONTINUUM MECHANICS
THERMAL ANALYSIS VARIANT

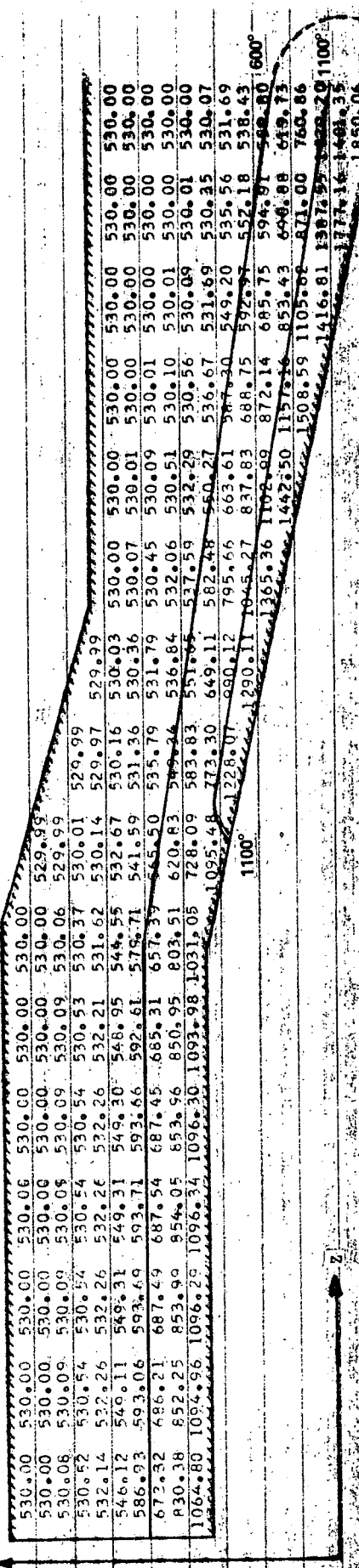
CASE 4 - ROCKET NOZZLE, 512 ELEMENTS, AXISYMMETRIC
ORNTN, KEY=1, EPS=0.001, KPPINIT=0, DELP=0.000028, HMIN=0.0, IF=0.00028
K=10.0, HC=VAR, TREE=6400, ALC=0.1

TIME = 0.000288 HOURS CURRENT INTEGRATION STEP SIZE = 0.21000E-04 HOURS

TEMPERATURE (DEGREES RANKINE)

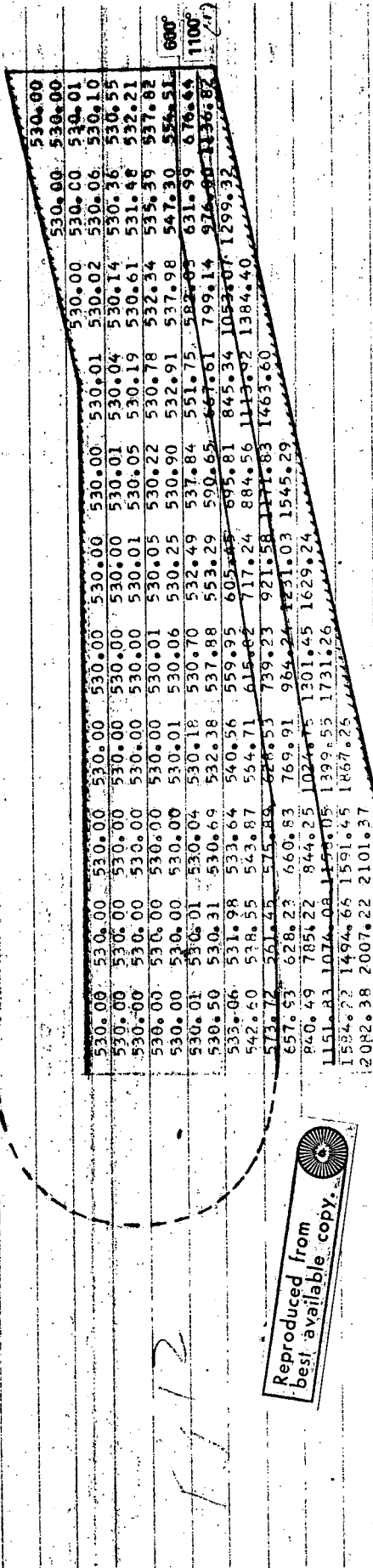
X1-COORDINATE (FT.)

0.02 0.03 0.05 0.07 0.08 0.10 0.12 0.13 0.15 0.16 0.17 0.17 0.17 0.18 0.19 0.20 0.21



X1-COORDINATE (FT.)

0.22 0.22 0.22 0.23 0.24 0.25 0.26 0.27 0.27 0.27 0.28 0.29 0.30



Reproduced from
best available copy.

Figure 12. Computed Temperature Distribution within Rocket Nozzle After One-Second Firing, 538 Finite Element Discretization

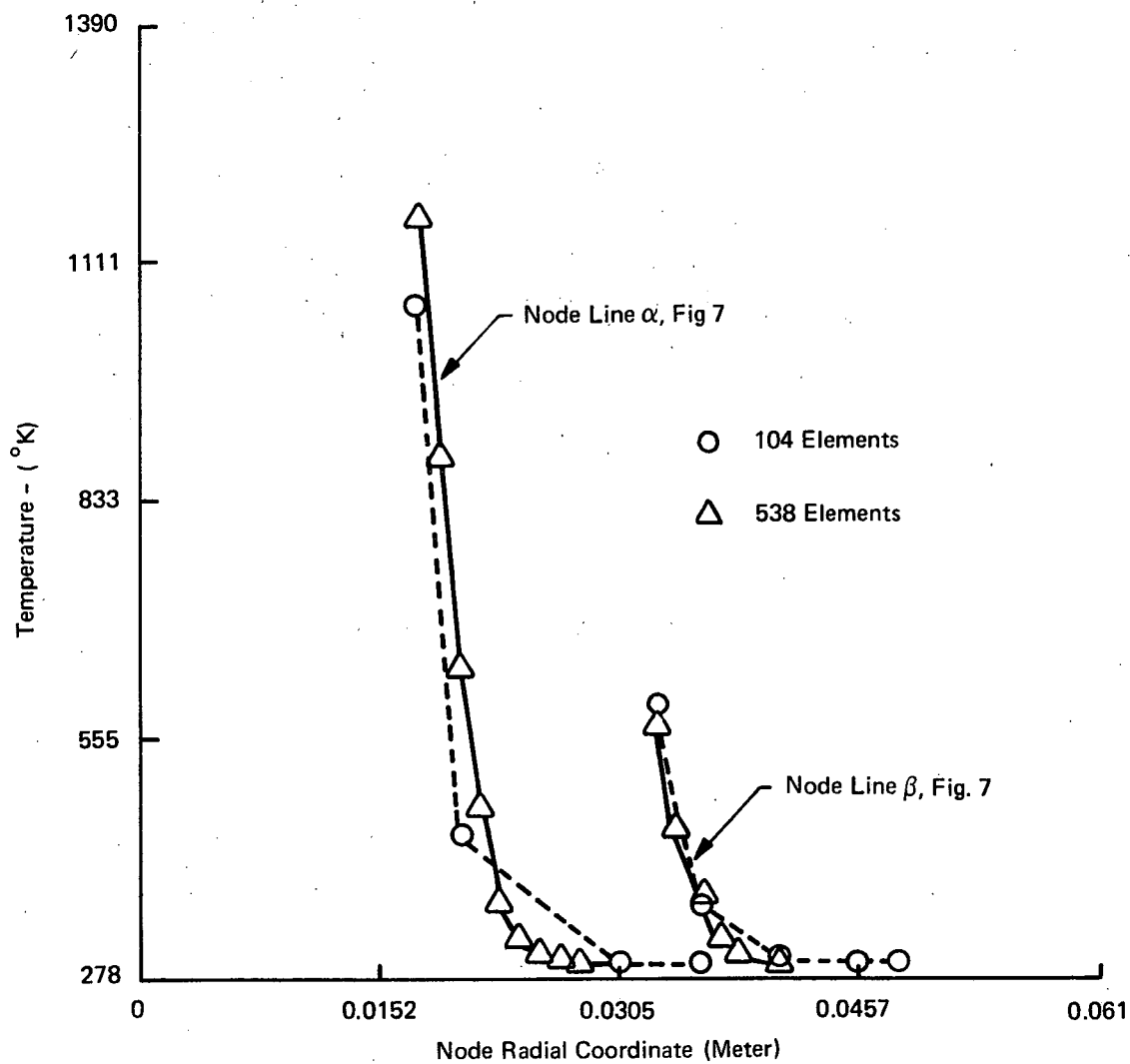


Figure 13. Computed Radial Temperature Distributions Through Rocket Nozzle Throat and Combustion Chamber After One Second Firing

Solution accuracy is affected by the integration method employed as well as discretization. The QKNINT package was adapted to allow the Euler integration algorithm (one-step, first-order accurate, predictor – no corrector), so favored by practicing engineers, to operate within the automatic error control features of QKNINT. Theoretical considerations (10) indicate that both of the QKNINT methods enjoy greater accuracy, as well as increased stability interval, as compared to the Euler method. Shown in Figure 14 is a comparison of the computed transient temperature solutions at the nozzle throat, for the 538 finite element discretization, during the first half second of firing. The smooth curve is faired through the QKNINT, Method 1 (QKNINT(1)) solution. The results of the Euler integration are observed to selectively lie above and below the QKNINT values to the maximum of $\pm 5.5^\circ\text{K}$ ($\pm 10^\circ\text{R}$). The differences are certainly small, but the QKNINT solution does appear smoother than the Euler predictions.

Evidence confirming that the QKNINT(1) solution can be more accurate is illustrated in Figure 15, which presents the computed nozzle surface temperature transient distribution, and the integration step size history for the two different integration methods and discretizations. The indicated surface temperature is faired through the square symbols, obtained with QKNINT(1) operating in the completely automatic mode, for the error parameter, $\epsilon = 0.01$, and for the integration step size history shown. The surface temperature distribution computed by QKNINT(1), starting with an initial step size three orders of magnitude larger than the automatic mode start, as illustrated by the circles, is essentially identical with the automatic mode results, and was obtained for the step size history illustrated. Therefore, the QKNINT(1) automatic mode results were obtained for integration step sizes well within the stability bounds of the integration algorithm. Integrating at step sizes nearer, but still within (by epsilon control) the bounds, did not degrade the solution.

The results of the Euler solution to the same problem, shown in Figure 15, indicate surface temperature predictions uniformly lower than the QKNINT (1) by up to 14°K (25°R). Concurrently, the Euler solution predicted somewhat higher solution temperatures along the exterior surface of the rocket motor, as illustrated by comparing Figures 16 and 17, which are computer output at the nine-second mark of the rocket firing. The step size history for the Euler test is also illustrated in Figure 15. Decreasing the error parameter to $\epsilon = 0.001$ did not measurably affect the predicted temperature history of either the Euler or QKNINT(1) solutions. Hence, from the proven convergence with discretization, and the results of the 538 element test case, the QKNINT(1) solution appears to enjoy greater accuracy than the Euler solution, in agreement with theory.

Shown for illustration purposes on Figure 15 is the transient temperature solution, through one second of the rocket motor problem, obtained for the 538 element discretization and QKNINT(1). It lies uniformly above the 104-element solution. The plotted step size history confirms the decreased stability of the differential equation system, Eq (2.21), resulting from use of a considerably finer solution domain discretization. Hence, the improved solution accuracy at the nozzle throat is obtained at a considerable increase in solution CPU time.

Shown in Table 6 are comparisons of computer CPU time for the standard 10-second firing of the 104-element rocket motor, as a function of integration algorithm and operation mode of QKNINT. The first entry, the standard for comparison, was obtained for completely automatic operation of QKNINT(1). The CPU time of 21.7 seconds was obtained for the case where the user provides no knowledge concerning the solution behavior to the computer program. The automatic determination of the minimum initial acceptable step size (HMIN) by QKNINT is conservative; inputting a larger HMIN, determined to be acceptable by experimentation, decreased solution time to 14.4 second CPU for QKNINT still operating under error control (defined as semiautomatic). This solution speed is comparable to the 13.9 sec CPU taken by Euler to integrate the same problem in the identical semiautomatic mode, i.e., input HMIN and operate under error control.

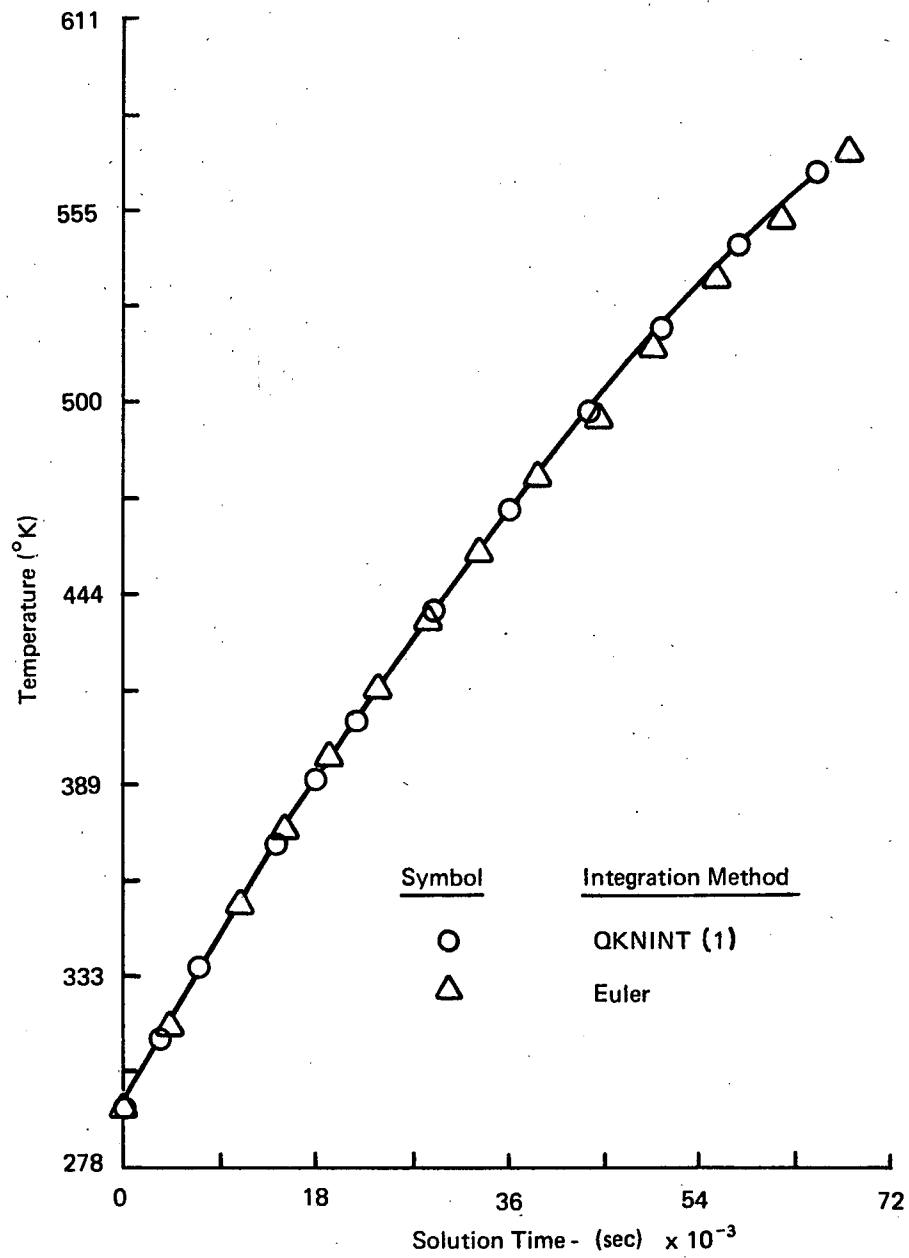


Figure 14. Comparison of Computed Transient Temperature Distribution at the Nozzle Throat for QKNINT Method 1 and Euler, 538 Finite Element Discretization

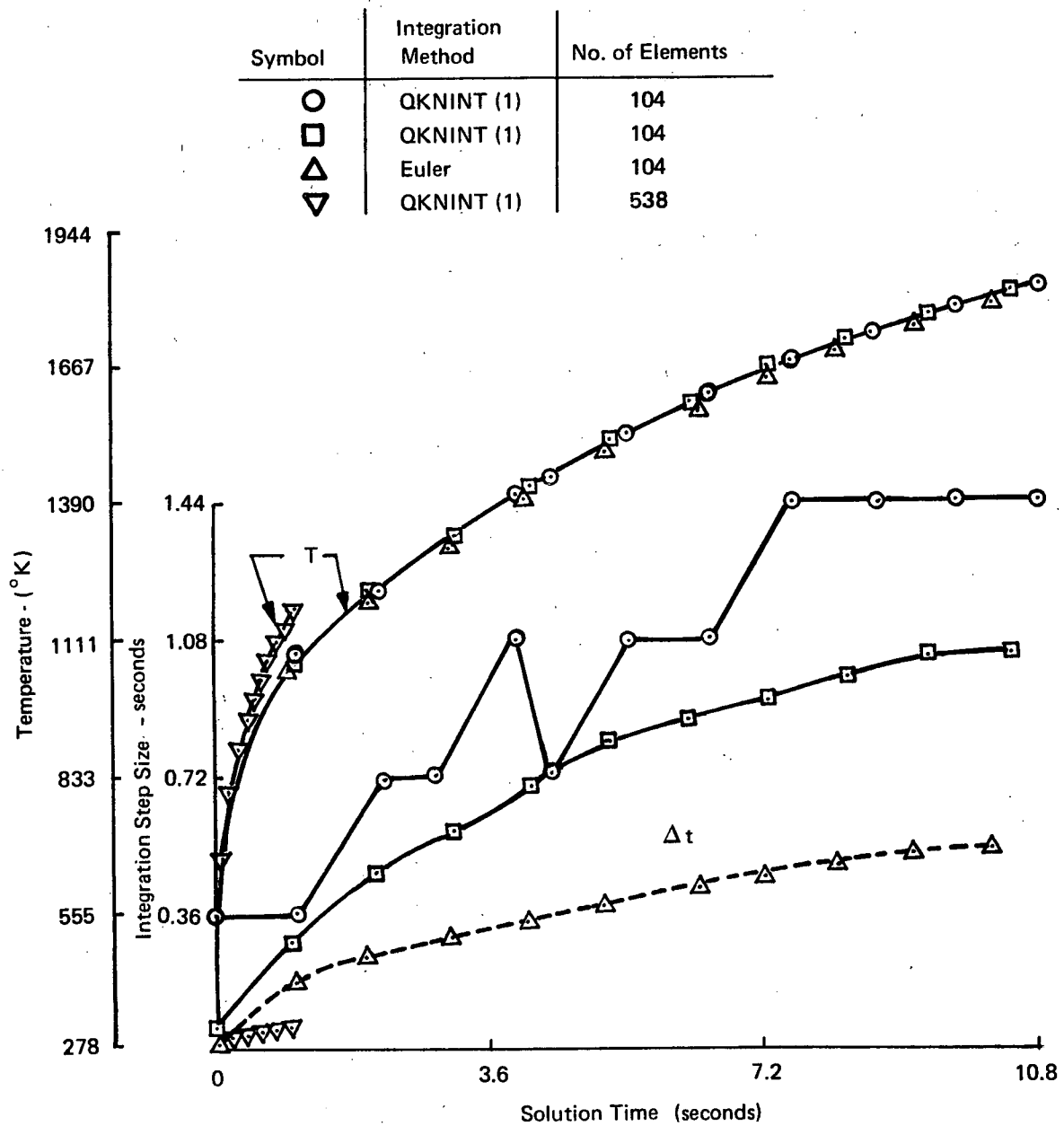


Figure 15. Comparison of Surface Temperature Distribution and Integration Step-Size History for QKNINT(1) and Euler, 104 and 538 Finite Element Discretizations, Epsilon = 0.01

C O M O C

COMPUTATIONAL CONTINUUM MECHANICS
THERMAL ANALYSIS VARIANT

CASE 3-1, ROCKET NOZZLE
QKNINT, KEY=3, EPS=0.01, KPRINT=1, DELP=.000288, HMIN=0., TF=.00288
K=10.0, HC=VAR, TREF=6460., ALC=0.1

TIME = 0.0026 HOURS CURRENT INTEGRATION STEP SIZE = 0.13200E-03 HOURS

X1-COORDINATE(FT.) 0.02 0.05 0.08 0.12 0.15 0.18 0.20 0.22 0.23 0.25 0.27 0.30

TEMPERATURE(DEGREES RANKINE)
653.29 661.00 657.48 641.46
689.86 690.47 686.15 669.88
740.00
955.84 932.95 923.07 896.52 778.45 781.16
828.68 830.90 750.91 703.67 702.71 741.04 794.03
1487.23 1448.26 1437.59 1402.63 1066.79 889.19 794.35 742.01 741.61 786.77 855.00
1823.96 1785.79 1777.46 1748.64 1165.40 1282.98 1142.14 1058.23 1060.60 1141.52 1262.97
1649.97 1099.59 1495.93
2025.82 1828.33 1785.21 1937.08
2248.38 2038.56 2224.08
2513.99 2323.25 2285.12 2491.28
2832.17 2620.21 2599.27 2809.10
3164.72 3151.73

TIME DERIVATIVE OF TEMPERATURE(NON-DIMENSIONAL)
0.04 0.06 0.06 0.05
0.10 0.18 0.18 0.17
0.05 0.04 0.13 0.04 0.04 0.04 0.04 0.04 0.04 0.04 0.04
0.09 0.23 0.23 0.21 0.19 0.14 0.12 0.11 0.11 0.12 0.12 0.12
0.03 0.07 0.07 0.07 0.20 0.07 0.12 0.05 0.21 0.26 0.23 0.19 0.11 0.04
0.02 0.03 0.08 0.06 0.02

QKNINT CUMULATIVE NUMBER OF TIMES STEP SIZE WAS DECREASED = 0 AND INCREASED = 34

Figure 16. Computed Temperature Distribution within Rocket Motor After Nine Second Firing Using Euler Integration Algorithm

COMPUTATIONAL CONTINUUM MECHANICS
THERMAL ANALYSIS VARIANT

CASE 3-1, ROCKET NOZZLE , DIAGONAL C-MATRIX, QKNWIN FACTOR=4.0
QKNINT, KEY=1, EPS=0.01 , KQRINT=1 DELP=.000288, HMIN=0. , TF=.00288
K=10.0, HC=VAR , TREF=6460. , ALC=0.1

TIME =	0.0024 HOURS	CURRENT INTEGRATION STEP	SIZE =	0.28800E-03 HOURS								
X1-COORDINATE(FT.)	0.02	0.05	0.08	0.12	0.15	0.18	0.20	0.22	0.23	0.25	0.27	0.30
TEMPERATURE(DEGREES RANKINE)												
650.12	657.73	654.29	638.41									
687.42	687.76	683.51	667.21									
956.39	932.98	923.95	896.27	736.28								
				776.12	776.98	825.98	744.25	696.33	695.57	735.76	789.33	725.01
					825.08	885.31	788.63	735.44	735.17	781.35	851.23	761.15
1490.97	1452.10	1441.36	1405.86	1066.65								908.81
1829.84	1791.08	1782.78	1753.78	1654.12	1165.88	1283.72	1140.98	1055.58	1057.84	1140.10	1263.64	1099.44
				2031.75	1832.54	2046.68						1498.86
					2258.96	2520.58	2330.78	2632.63	2611.09	2293.54	2028.53	1789.60
							2853.88	3185.23	3175.87	2829.57	2505.06	1842.97

[illegible]

	CUMULATIVE NUMBER OF TIMES STEP SIZE WAS DECREASED =	1 AND INCREASED =	21
QKNINT			

Figure 17. Computed Temperature Distribution within Rocket Motor After Nine Second Firing Using QKNINT (1) Integration Algorithm

TABLE 6
COMPARISON OF SOLUTION SPEED FOR QKNINT (1) AND EULER,
EPSILON = 0.01

Symbol Figure 15	No. of Elements	Integration Method	Operating Mode	CPU Time Seconds	Integration Step-Size Extremum, sec.		TFINAL sec.
					H min	H max	
<div>□</div> <div>⊙</div> <div>△</div>	104	QKNINT (1)	Automatic	21.7	0.0596	1.092	10.4
	104	QKNINT (1)	Semiautomatic	14.4	0.360	1.440	10.8
	104	EULER	Semiautomatic	13.9	0.0144	0.532	10.1
	104	QKNINT (1)	Manual	11.6	0.360	1.440	10.8
	104	QKNINT (1)	Manual	8.9	0.360	1.440	1.08
	104	QKNINT (1)	Manual	22.7	0.360	0.360	10.4
	104	QKNINT (1)	Automatic	47.6*	0.0144	0.461	10.4
	532	QKNINT (1)	Automatic	162.0	0.0036	—	01.08

*Epsilon = 0.001

The semiautomatic QKNINT (1) run established lower bounds on acceptable step size history. Using the semiautomatic step-size distribution, and going to completely manual operation (no error control), reduced CPU time to 11.6 sec, a 19% reduction over QKNINT (1) semiautomatic and 16% less than Euler. A 36% reduction over Euler to 8.9 sec CPU was accomplished by manual QKNINT (1) operating uniformly at HMAX of the semiautomatic mode, except for the first integration step taken at HMIN. Solution accuracy was essentially identical to semiautomatic QKNINT (1). As illustration that testing in automatic QKNINT (1) is not optimal, a run was made at constant step size equal to input HMIN. The CPU time comparison of 22.7 seconds is just measurably larger than the completely automatic case which attained a maximum step size (HMAX) four times larger than HMIN. Decreasing epsilon to 0.001 increased CPU time to 47.6 seconds for QKNINT (1) automatic mode, and did not measurably affect the solution. The one-second firing of the 538 element discretization required 162 seconds CPU for QKNINT (1) automatic. Finally, the CPU time for the QKNINT (1) fully automatic, 104-finite-element discretization solution was a factor of five smaller than the comparison "finite difference" computer program, which employs an Euler integration procedure.

The solution speed for the completely automatic operation mode of QKNINT was found to depend quite strongly on the internal algebraic factor by which current step-size is multiplied during the seeking process for HMIN. Shown in Figure 18 is the comparison of CPU time to process the standard rocket motor test case as a function of the HMIN seeking factor. The optimum value for the factor appears to be in the range $3\frac{1}{2}$ to 4. On either side, a too conservative estimate of HMIN is found with a resultant increase in CPU time for execution. The automatic mode in QKNINT presently employs a factor of 4. It has similarly been determined that requesting output at exact time stations, which requires internal interpolation, can increase CPU time by 10-20% dependent upon the problem.

COMOC operates independent of whether the problem is two-dimensional or axisymmetric. Shown in Figure 19 is the computed temperature distribution for the rocket motor initial and boundary conditions and geometry, except for a two-dimensional problem specification, after 9 seconds of solution time. Comparing the results to Figure 17 shows that overall higher temperatures are computed; however, the stability character of the two-dimensional equations is essentially identical to the axisymmetric problem, with both automatically establishing an identical HMIN and requiring the same CPU time for execution.

C. VERSATILITY ILLUSTRATION FOR COMOC

The COMOC heat transfer variant enjoys considerable versatility for diverse problem categories in addition to the basic boundary condition generality. Inclusive features are element specifiable internal heat generation (or removal), general tensor thermal conductivity, variable element thicknesses in two-dimensional problems, and multi-material capability, each with specifiable thermophysical properties.

The transient temperature history of the rocket motor has been illustrated. A disastrous manufacturing defect, amounting to an internal void located behind the nozzle throat, was simulated by identifying a new material with zero thermal conductivity in the immediate throat neighborhood elements located between Node Rows B-B', Figure 7. The computed solution remained stable in automatic mode operation, and the throat surface temperature indicated burn-out after only three seconds of firing.

One might intuitively estimate that placing an insulator on the exterior rocket surface would raise nozzle surface temperatures. The thermophysical properties of elements between Node Rows C-D, Figure 7, were changed to simulate asbestos and the ten second firing repeated. Interestingly, the nozzle surface temperature was not measurably altered, while the exterior surface temperatures (Node Row D) remained essentially at the initial 294°K value. Only the temperatures along Node Row C were increased, by a maximum of about 75°K.

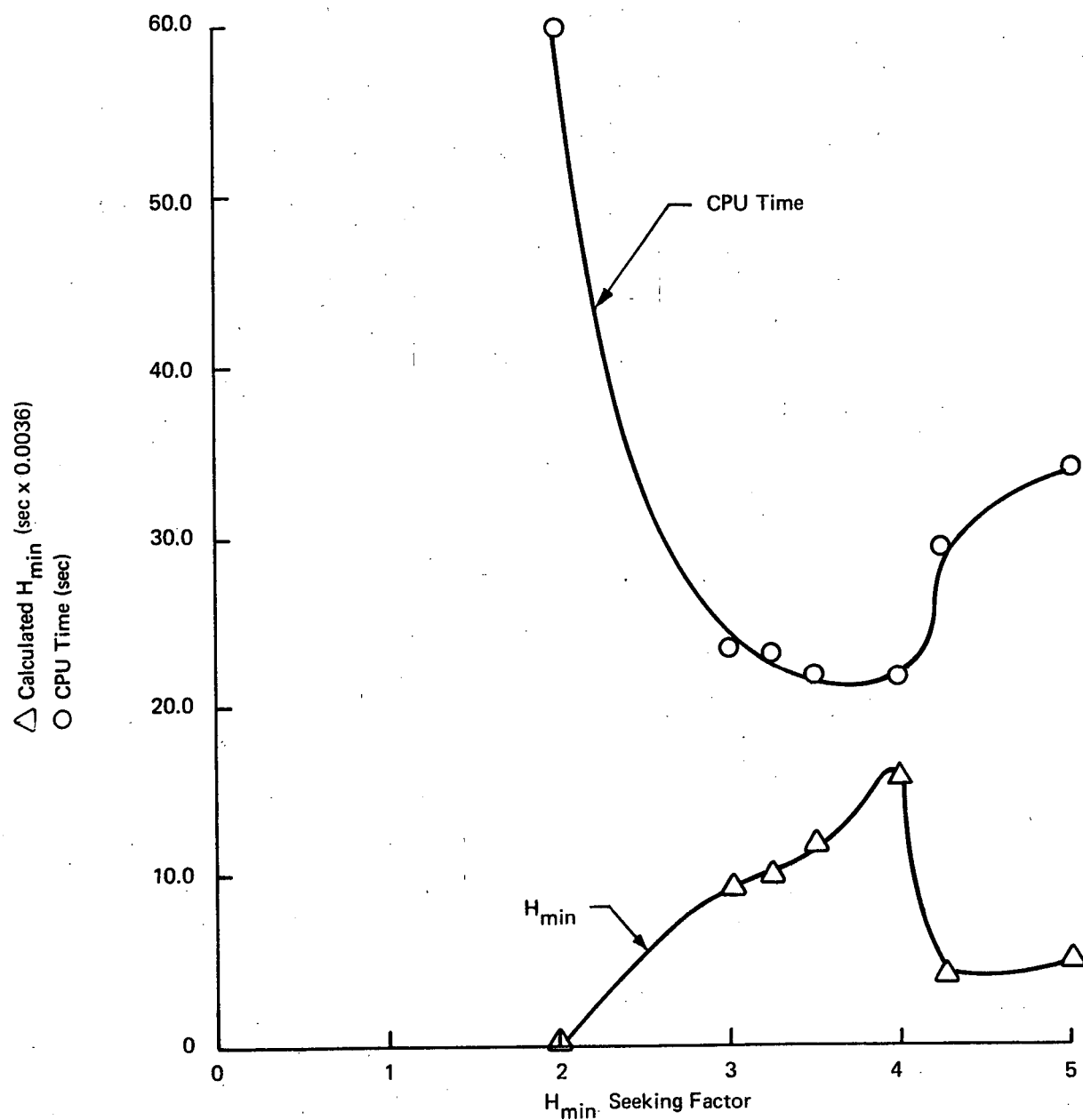


Figure 18. Solution Speed as Function of HMIN Seeking Factor For Automatic Operation Mode of QKNINT

C O M O C
COMPUTATIONAL CONTINUUM MECHANICS
THERMAL ANALYSIS VARIANT

CASE 3-1, ROCKET NOZZLE
QKNINT, KEY=1, EPS=0.010, KPRINT=0 DELP=.00028, HMIN=0.0, TF=.0028
K=10.0, HC=VAR, TREF=6460., ALC=6.1

TIME = 0.0026 HOURS				CURRENT INTEGRATION STEP SIZE = 0.28800E-03 HOURS											
X1-COORDINATE(FT.)				0.02	0.05	0.08	0.12	0.15	0.18	0.20	0.22	0.23	0.25	0.27	0.30
TEMPERATURE(DEGREES RANKINE)															
679.19	687.77	683.71	664.21												
724.05	723.93	719.00	699.55	783.08											
1027.90	1003.41	993.88	964.71	832.02	838.22									782.80	688.96
					898.41				910.18	822.77	768.99	767.22	811.07	867.49	741.24
1579.98	1544.55	1534.18	1501.39	1167.77		984.67	881.71	823.24	821.85	871.12	944.26				
1909.61	1875.52	1867.42	1842.71		1294.26									1223.66	1003.44
				1786.60		1449.55	1315.23	1233.07	1233.13	1309.94	1424.92				
				2156.76										1947.80	1638.88
					1994.72										
					2409.47	2250.88								2378.56	2074.41
						2707.50	2584.28						2552.09		
							3079.25	2935.44	2919.37	3059.70					
								3443.76	3434.74						

TIME DERIVATIVE OF TEMPERATURE(NON-DIMENSIONAL)													
0.00	0.01	0.01	0.01										
0.01	0.02	0.02	0.02										
				0.01	0.03	0.01	0.01	0.01	0.01	0.01	0.01	0.01	0.01
0.02	0.04	0.04	0.04	0.01	0.02	0.02	0.02	0.02	0.02	0.02	0.02	0.02	0.02
				0.04	0.04	0.04	0.04	0.04	0.04	0.04	0.04	0.04	0.04
0.02	0.04	0.03	0.03	0.03	0.03	0.03	0.03	0.03	0.03	0.03	0.03	0.03	0.03
0.00	0.01	0.01	0.01	0.01	0.01	0.01	0.01	0.01	0.01	0.01	0.01	0.01	0.01

QKNINT
CUMULATIVE NUMBER OF TIMES STEP SIZE WAS DECREASED = 1 AND INCREASED = 21

Figure 19. Computed Temperature Distribution in Two-Dimensional Analog of Axisymmetric Rocket Motor Problem

Of significant engineering design value would be evaluation of candidate methods for reducing throat temperatures. Of course, using a higher conductivity material with adequate strength properties, if available, would accomplish the desired reduction. A more feasible solution would be to install a high thermal conductivity insert into the nozzle throat region and keep the remainder of the motor stainless for strength. The throat region interior to the small cross-hatched border, Figure 7, was changed to the material properties of graphite, and the ten second firing repeated. Shown in Figure 20 are radial temperature distributions with and without the insert, at axial stations at the throat (Node Line α , Figure 7), along the graphite-stainless interface upstream of the throat ($z = 0.055$ m), and within the stainless further upstream of the throat ($z = 0.051$ m). A definite knee in the temperature is observed at the graphite-stainless interface on Node Line α , Figure 20. The throat surface temperature is approximately 60°K cooler, at that time in the firing, while the material behind the throat is appropriately somewhat hotter. A smaller temperature difference is noted, Figure 20, at the upstream graphite-stainless interface. It is noteworthy that COMOC computes temperatures at node points lying on a line of material discontinuity with no requirement for any user guidance. The final temperature distribution in Figure 20 verifies that the extra heat removed by the graphite insert at the throat is conducted throughout the remainder of the motor.

A promising variation is the hypothesis that the motor be made from material in every regard stainless except for its radial thermal conductivity, which approximates that of graphite, i.e., material possessing a favorable thermal conductivity tensor. Shown in Figure 21 is the comparison of the axial temperature distributions after a ten-second firing for the stainless and pseudo-stainless orthotropic conductivity rocket motor. A dramatic reduction in interior surface temperature is computed everywhere upstream of the throat at the expense of significantly increased temperature levels at the nozzle terminus. These results indicate that if such a material were available it might be ideal for rocket motor construction.

Active cooling, by the passage of propellant through drilled passages near the interior surface of the rocket motor, is a proven method for reducing temperature levels in the nozzle throat region. Such a problem description is truly three-dimensional; however, a two-dimensional simulation of cooling could yield informative design guidance. As an illustration, an extra row of nodes was placed parallel to and just exterior, to Node Row B, Figure 7. Additional discretization was added to form a band of triangular elements directly behind those on the interior surface, and the presence of active fluid cooling simulated by applying negative heat addition therein. Shown in Table 7 is the comparison of computed radial temperature distributions along Node Line α , Figure 7, resulting from various levels of simulated active cooling of the rocket motor during the 10 second firing.

The ability of COMOC to accept a finite element thickness distribution for two-dimensional problems renders it applicable to problems where three-dimensional effects exert a prominent influence but for which a full three-dimensional solution is not warranted. As an illustration, the 104 element rocket motor discretization was considered as the plane cross section of material that had a 2:1 thickness variation over its length (the z axis, Figure 7). Welding was assumed to have occurred between Node Rows A and B, Figure 7, within the region $0.046 \leq z \leq 0.061$ m. The surface temperature distribution occurring 10 seconds after cool down was initiated is shown in Figure 22. The smaller slope of temperature in the thicker region (to the right of the weld centerline) is quite apparent from the dashed mirror image overlay.

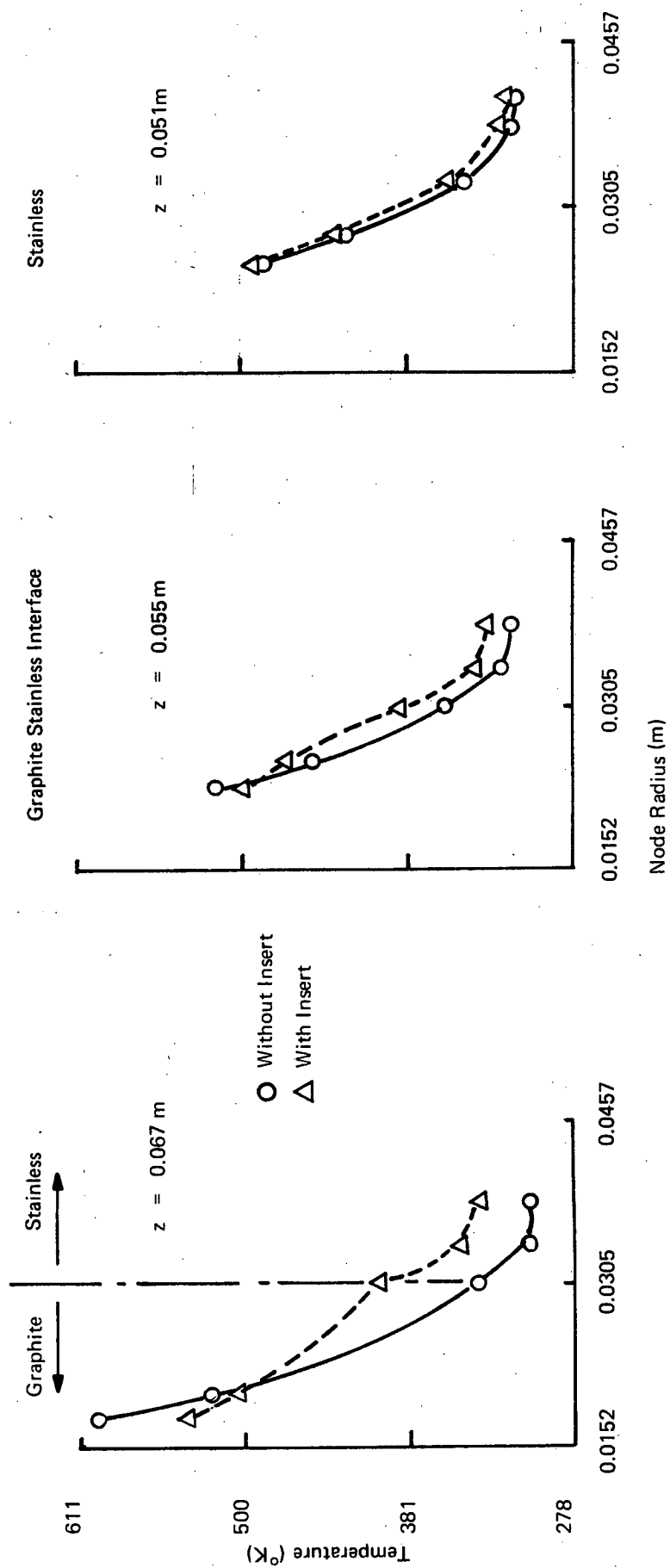


Figure 20. Radial Temperature Distribution Comparison for Graphite Insert and Stainless Steel Rocket Motor

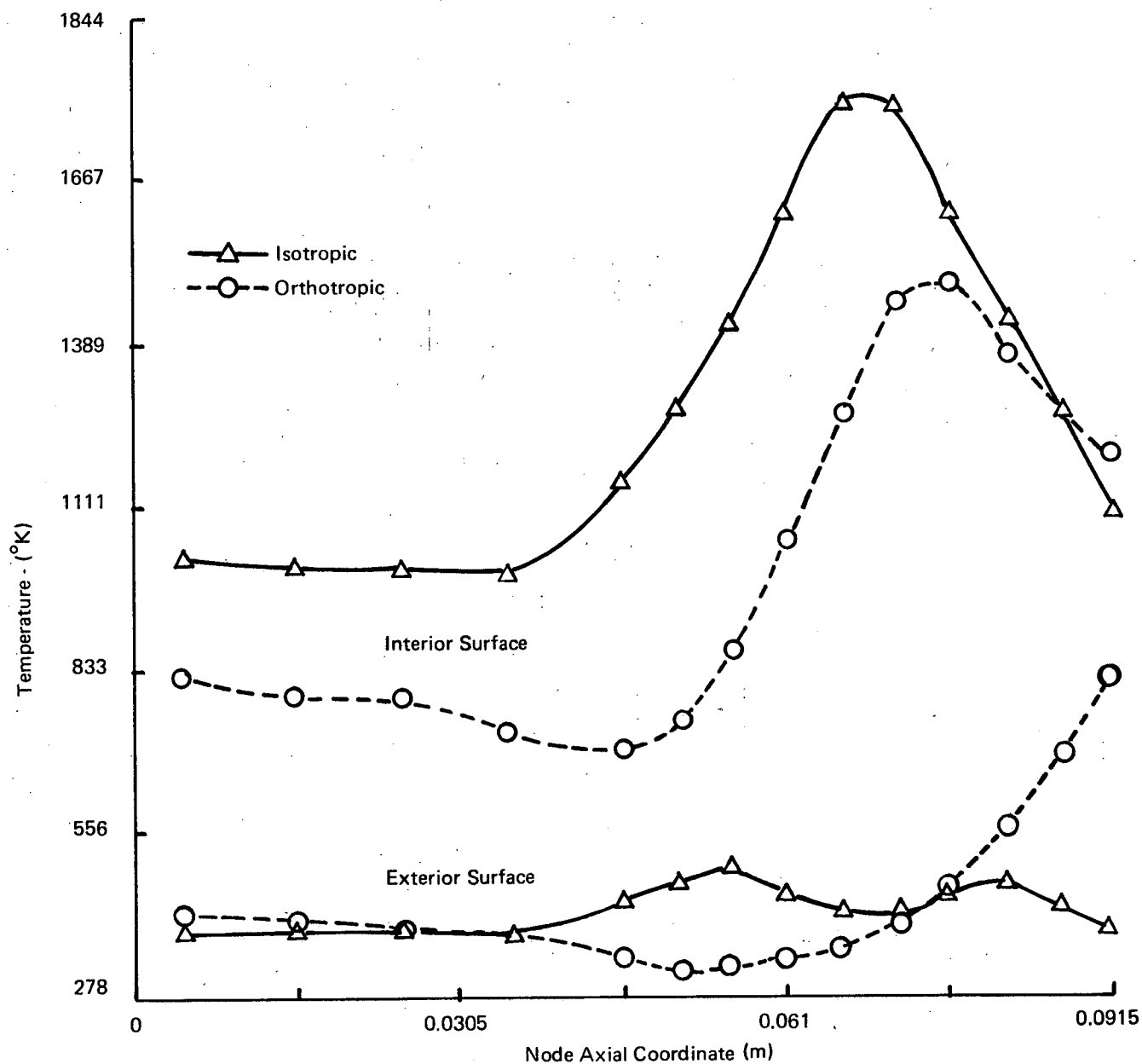


Figure 21. Computed Rocket Motor Surface Temperature Distributions After 10 Second Firing for Isotropic and Orthotropic Thermal Conductivities

TABLE 7

COMPUTED RADIAL TEMPERATURE DISTRIBUTION
ALONG NODE LINE α , FIGURE 7, FOR SIMULATED ACTIVE COOLING
OF ROCKET MOTOR AFTER 10 SECOND FIRING

Node Sequence Node Line α	Temperature °K (°R)					
	Simulated Active Cooling Rates – W/m ² (BTU/hr ft ²)					
	0		3.15 x 10 ⁵ (10 ⁶)		3.15 x 10 ⁶ (10 ⁷)	
1	1810	(3255)	1804	(3245)	1770	(3185)
2	1511	(2720)	1503	(2706)	1460	(2626)
3			999	(1780)	940	(1690)
4	637	(1145)	616	(1109)	587	(1054)
5	453	(798)	430	(774)	416	(747)
6	420	(755)	400	(729)	392	(706)

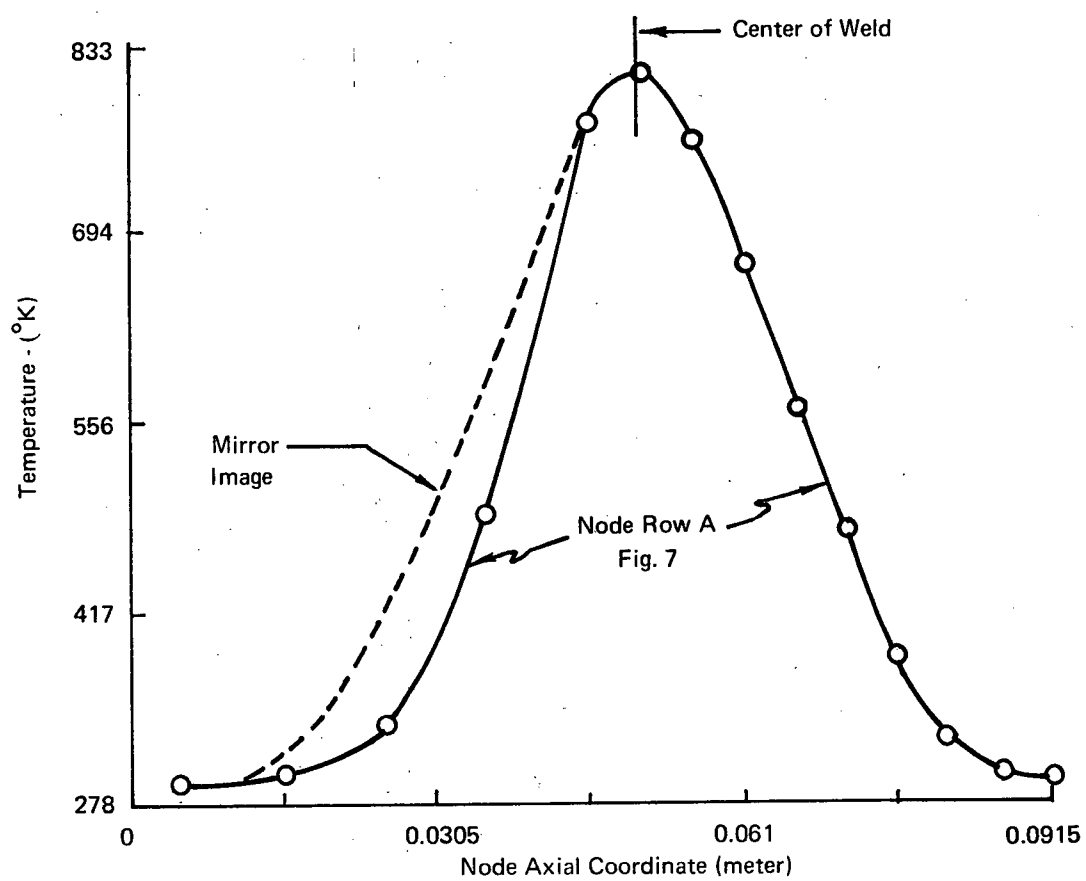


Figure 22. Axial Surface Temperature Distribution 10 Seconds After Welding Operation on Segment of Wedge Shaped Domain

VI. CONCLUSIONS AND RECOMMENDATIONS

The documented computational experiments with the Thermal Analysis Variant of the COMOC computer program system have conclusively demonstrated the considerable versatility, engineering usefulness, computational efficiency, and mathematical soundness of the computational embodiment of a finite element solution algorithm for solution of transient problems of energy conservation in stationary, multi-material continua. Considerable computational speed is indicated using a highly-stable explicit numerical integration procedure, for problems of practical engineering importance involving complex geometrical shapes and nontrivial boundary condition specifications. The ease with which output can be oriented for quick engineering evaluation has been demonstrated. As a system, COMOC appears to effectively communicate to the practicing design engineer the sophisticated numerical mathematics of modern day digital computing software systems.

As a natural consequence of the considerable numerical experimentation performed in the development of COMOC, several areas have emerged in which the performance of the computer program system could be improved:

1. It is apparent that testing for solution accuracy in QKNINT is costly, and that the error-dictated discarding of entire integration steps is a major contributing factor. A recently completed theoretical study indicates that the accuracy test could be performed at the end of the prediction step rather than after the second correction step. With such a change in QKNINT, epsilon becomes actual percentage error. More importantly, from the economy standpoint, a too large integration interval is determined with one-third the execution time of the presently employed method. This would not materially affect CPU time for accepted integrations, but would decrease by up to 40% the CPU time required to complete an integration at a reduced step-size. This improvement is experimentally verified, as detailed in Table 6, for the QKNINT (1) manual mode experiments, which decreased by 19% the CPU time of the semi-automatic mode solution while marching at the identical step-size distribution.
2. It is quite apparent that the high stability methods in QKNINT are capable of generating accurate solutions using integration step-sizes that are comparable to, and may actually exceed, the desired output print intervals. If the solution accuracy of an Euler integration is acceptable, the QKNINT package could be readily adapted to automatically switch over to Euler when output requirements constrain the integration step size below the stability limit of the highly stable method. A significant savings in CPU execution time could then result for problems that are output-bound while retaining the automatic error control features within the QKNINT package.
3. The natural coordinate formulation for finite element matrices has improved accuracy and the speed of matrix computation in comparison to previously employed techniques. The extension of COMOC to full three-dimensionality using these functional representations is very straightforward and will considerably expand its applicability. At the same time, COMOC could be extended to handle problems involving a mix of two- and three-dimensional elements such that complex aerospace geometries could be readily and economically analyzed.
4. Active cooling of aerospace structures is of paramount importance in many applications, e.g., laser mirrors and hypersonic aerodynamic panels. The finite element formulation for energy conservation is readily extended to include a "fluid cooling element" by enforcing both mass and energy conservation, for the additional (fluid) material specification within the solution domain. The directional character of

the fluid flow would be automatically enforced by the convective additions to the [K] matrix system. Hence, an accurate accounting of heating of the coolant and the resultant temperature distribution within the containing structure would result. The addition of such a "fluid element" capability within COMOC, in either two- and/or three-dimensional space would provide a uniquely powerful analysis tool for economical engineering design studies of complex aerodynamic and aerospace hardware systems.

VII. REFERENCES

1. The MacNeal-Schwendler Corp., "NASTRAN Heat Transfer Capability: Theoretical Development and Functional Module Mathematical Specification," Report MS154-1, Dec. 1971.
2. Zienkiewicz, O.C., "The Finite Element Method in Engineering Science," McGraw Hill, London, 1971, Chapter 7.
3. Crane, R.L., and Klopfenstein, R.W., "A Predictor-Corrector Algorithm with an Increased Range of Absolute Stability," J. ACM. 12, 2 (April 1965), 227-241.
4. Lawson, J.D., "An Order Five Runge-Kutta Process with Extended Region of Stability," SIAM J. Numer. Anal. 3, 4 (Dec. 1966), 593-597.
5. Lawson, J.D., "An Order Six Runge-Kutta Process with Extended Region of Stability," SIAM J. Numer. Anal. 4, 4 (Dec. 1967), 620-625.
6. Rahme, H.S., "A New Look at the Numerical Integration of Ordinary Differential Equations," J. ACM. 16, 3 (July 1969), 496-506.
7. Nigro, B.J., "An Investigation of Optimally Stable Numerical Integration Methods with Application to Real-Time Simulation," Simulation 13, 5 (Nov. 1969), 253-264.
8. Nigro, B.J., Woodward, R.A., Brucks, C.R., "A Digital Computer Program for Deriving Optimum Numerical Integration Techniques for Real-Time Flight Simulation," Aerospace Medical Research Laboratory Report, AMRL-TR-68-4, AD673372, May 1968.
9. Nigro, B.J., "The Derivation of Optimally Stable, K-Stage, One-Step, Explicit Numerical Integration Methods," Bell Aerospace Company Technical Note TCTN 1008, April 1970.
10. Nigro, B.J., "The Derivation of Optimally Stable, Three-Stage, One-Step Explicit Numerical Integration Methods," Bell Aerospace Company Technical Note TCTN-1010, August 1971.
11. Baker, A.J., "Finite Element Solution Algorithm for Viscous Incompressible Fluid Dynamics," to be published in Int. J. Num. Mth. Engr.
12. Baker, A.J., "Finite Element Computational Theory for Three-Dimensional Boundary Layer Flow," AIAA Preprint No. 72-108, January 1972.
13. Baker, A.J., "A Finite Element Computational Theory for the Mechanics and Thermodynamics of a Viscous, Compressible Multi-Specie Fluid," Bell Aerospace Research Report 9500-920200, June 1971.
14. Bauer, A.M., and Baker, A.J., "COMOC-Thermal Analysis Variant; User's Manual," Bell Aerospace Research Report 9500-920256, October 1972.
15. Zienkiewicz, O.C., and Cheung, Y.K., "Finite Elements in the Solution of Field Problems," The Engineer, Sept. 24, 1965, 507-510.

16. Wilson, E.L., and Nickell, R.E., "Application of the Finite Element Method to Heat Conduction Analysis," Nuc. Engr. Design, 4, 1966, 276-286.
17. Biot, M.A., "Further Developments of New Methods in Heat-Flow Analysis," J. Aero. Sci., 26, 1959, 367.
18. Gurtin, M.E., "Variational Principles for Linear Initial-Value Problems," Q. App. Math, 22, 1964, 252.
19. Baker, A.J., "A Numerical Solution Technique for Problems in Heat Transfer Employing the Calculus of Variations," Bell Aerospace Technical Note TCTN-1003, April 1968.
20. Finlayson, B.A., and Scriven, L.E., "The Method of Weighted Residuals - A Review," App. Mech. Rev., 19, No. 9, 1966, 735-748.
21. Finlayson, B.A., and Scriven, L.E., "On the Search for Variational Principles," Int. J. Heat Mass Trans., 10, No. 6, 1967, 799-821.
22. Gallagher, R.H., and Mallett, R., "Efficient Solution Processes for Finite Element Analysis of Transient Heat Conduction," ASME Preprint 69-WA/HT-32, Nov. 1969.
23. Rybicki, E.F., and Hopper, A. T., "Higher Order Finite Element Method for Transient Temperature Analysis of Inhomogeneous Materials," ASME Preprint 69-WA/HT-33, Nov. 1969.
24. Aguirre - Ramirez, G., and Oden, J.T., "Finite Element Technique Applied to Heat Conduction in Solids with Temperature Dependent Thermal Conductivity," ASME Preprint 69-WA/HT-34, Nov. 1969.
25. Richardson, P.D., and Shum, Y.M., "Use of Finite Element Methods in Solution of Transient Heat Conduction Problems," ASME Preprint 69-WA/HT-36, Nov. 1969.
26. Brocci, R.A., "Analysis of Axisymmetric Linear Heat Conduction Problems by Finite Element Method," ASME Preprint 69-WA/HT-37, Nov. 1969.
27. Emery, A.F., and Carson, W.W., "Evaluation of Use of the Finite Element Method in Computation of Temperature," ASME Preprint 69-WA/HT-38, Nov. 1969.
28. Mason, J., "Optical Telescope Technology," NASA SP-233, 1969.
29. Rosette, K.L., Mason, J., Jarrell, T.W., "Structural Thermal Optical Program (STOP) Phase I, Results of Feasibility Study to Investigate Use of Analytical Techniques to Evaluate Thermal Elastic Response of Space Structures," Dirs. 01486, NASA Goddard Space Flight Center, 1968.
30. Zienkiewicz, O.C., and Parekh, C.J., "Transient Field Problems: Two-Dimensional and Three-Dimensional Analysis by Isoparametric Finite Elements," Int. J. Num. Mtd. Engr., 2, 1970, 61-71.
31. Carslaw, H.S., and Jaeger, J.C., "Conduction of Heat in Solids," 1st Ed., Oxford, London, 1948, 275.
32. Baker, A.J., "On a Correlation Between 'Finite Difference' and 'Finite Element' Heat Transfer Analysis . . .," Bell Aerospace Technical Note TCTN-1007, Nov. 1969.